Effect of surfactant on drop dynamics in linear flows.

Petia M. Vlahovska*, Jerzy Blawzdziewicz' and Michael Loewenberg"
* Division of Engineering, Brown University; ' Mechanical Engineering, Yale University; " Chemical Engineering, Yale University

1 Introduction

Predicting emulsion rheology requires understanding the coupled drop deformation and surfactant dynamics in flow. The problem is challenging because of the ability of drop shape and surfactant to undergo flow-induced deformations; drop shapes and surfactant distribution are not given *a priori* but are governed by the balance of viscous and interfacial stresses. Adsorbed surfactant reduces the interfacial tension and thus increases deformation in order to satisfy the normal stress balance. Nonuniformities in the surfactant concentration give rise to gradients in the interfacial tension along the surface (Marangoni stresses) that oppose deformation. The result is an intricate interplay between surfactant redistribution, drop deformation and bulk flows.

Experimental studies [1, 2, 3, 4, 5] show quantitatively and qualitatively different picture of drop deformation in presence of surfactant compared to the surfactant-free case. However, theoretical analyses are at early stage.

In this paper we present results for the effective stress of an emulsion of surfactant covered drops. A compact perturbation solution for the deformation of a surfactant-covered drop, suspended in a fluid of the same viscosity, subjected to an arbitrary linear flow is developed. A third order perturbation solution for small deviations from sphericity is explicitly derived. A forthcoming paper considers the effect of the viscosity contrast on drop deformation.

2 Dynamics of a drop in Stokes flow

We consider a Newtonian drop with radius a and viscosity η, suspended in a Newtonian fluid with the same viscosity. Creeping flow conditions are assumed. A dilute surfactant monolayer is present on the drop interface; the surfactant is insoluble in the bulk phases, i.e. a fixed amount of surfactant is adsorbed onto the drop interface. The average surfactant concentration on the drop interface is $\Gamma_{\rm eq}$. The corresponding interfacial tension is $\sigma_{\rm eq}$, and σ_0 is the interfacial tension in the absence of surfactant.

The flow distorts the drop shape and redistributes the surfactant. The magnitude of the deformation is characterized by two dimensionless parameters. The capillary number compares the strength of the distorting viscous stresses to the restoring interfacial stresses

$$Ca = \frac{\sigma_{\rm eq}}{\eta a \dot{\gamma}}\,. \tag{1}$$

Likewise, the Marangoni number compares the viscous stresses to the Marangoni stresses (gradients in interfacial tension)

$$Ma = \frac{\eta a \dot{\gamma}}{\Delta\sigma}. \tag{2}$$

Drop shape remains close to spherical provided that the capillary number is small; surfactant distribution remains close to the equilibrium uniform one if the Marangoni number is large. A measure for the stiffness of the surfactant layer is the elasticity number

$$E = Ma\, Ca. \tag{3}$$

In a coordinate system centered at the drop, the radial position $r_{\rm s}$ of the drop interface can be represented as

$$r_{\rm s} = \alpha + \varepsilon f(\Omega)\,, \tag{4}$$

where Ω is the solid angle and f is the deviation of drop shape from sphericity, which depends only on the angle Ω. The isotropic contribution α is given by the volume conservation constraint

$$\int (\alpha + \varepsilon f)^3\, d\Omega = 4\pi, \tag{5}$$

with the integration performed over the unit sphere.

The magnitude of the perturbation is scaled by a dimensionless parameter ε, the particular choice of which depends of the nature of the problem under consideration [6]. For example, in weak flows a suitable choice for ε is the capillary number, Ca.

3 Weak flow expansions

In this section we provide explicit expressions for the stresses expansions in the case of simple shear flow.

3.1 Surfactant–free drop

For surfactant-free drops our third order solution recovers the second-order results reported by Barthes-Biesel and Acrivos [7]. The expansion for the shear stress is

$$T_{12} = \frac{7}{4} - Ca^2 \frac{2107}{512}, \tag{6}$$

and for the normal stress differences

$$\begin{aligned} N_1 =& Ca\frac{245}{32} - Ca^3\frac{249361}{442368}, \\ N_2 =& -Ca\frac{35}{16} - Ca^3\frac{19440211}{14598144}, \end{aligned} \tag{7}$$

3.2 Surfactant–covered drop

The expansions for the steady state stresses are

$$\begin{aligned} T_{12} =& \frac{5}{2} - Ca^2\frac{25\left(98+98E+239E^2\right)}{1176E^2}, \\ N_1 =& Ca\frac{5\left(4E+1\right)}{2E} - Ca^3\frac{5\left(2940+5789E+8103E^2+7114E^3\right)}{7056E^2}, \\ N_2 =& -Ca\frac{5\left(13E+7\right)}{28E} + Ca^3\frac{5\left(8602440+2124199E-3147942E^2+8390519E^3+2587200E^4\right)}{8692992E^2}. \end{aligned} \tag{8}$$

4 Results

Our results indicate that under weak-flow conditions a surfactant-covered drop deforms only slightly more than a surfactant-free drop, as observed experimentally [8, 5]. Shape deformation is relatively insensitive to the elasticity of the surfactant layer. The leading order small deformation solution indicates that $f \sim Ca$ (and independent of the elasticity number E).

Even though in weak flows surfactant effect on drop shape deformation is small, surfactant redistribution on the drop interface depends strongly on the elasticity. As a result the emulsion rheology is significantly affected by the presence of surfactant.

Figure 2 illustrates the shear thinning behavior of an emulsion of deformable drops covered with surfactant monolayers of different elasticities. The shear viscosity decreases with the increase of the shear rate. At low flow strengths, the surfactant immobilizes the interface and the emulsion behaves as a suspension of hard spheres. For drops covered with a low elasticity surfactant film, the shear viscosity approaches quickly to the surfactant-free drop behavior, because in stronger flows the surfactant is passively convected on the drop surface.

Shear thinning and normal stresses are quantitatively predicted by the small deformation theory, as shown on Figure 3 for the normal stresses. In comparison, the linear theory [8] predicts zero normal stresses.

Truncating the expansions (8) at Ca^3 provides more accurate results for the normal stresses compared to the shear stress. This explains the poorer agreement between the analytical and numerical results for the shear stress, as seen in Figure 2, compared to the normal stresses.

5 Conclusions

A perturbation solution of order $O\left(\varepsilon^2, \varepsilon^3 Ca^{-1}, \varepsilon^3 Ma\right)$, where ε measures the magnitude of the shape distortion, was derived to describe the deformation of a surfactant-covered drop in linear viscous flows. Expressions for the shape and surfactant evolution equations, as well as stress and velocity fields were developed. The solution is applicable for any linear flow, both transient or steady state state conditions.

Predictions of the small deformation theory for drop shape, surfactant distribution as well as emulsion rheology are in quantitative agreement with the numerical simulations, and in qualitative agreement with experimental data.

References

[1] A. Williams, J. J. M. Janssen, and A. Prins. Behaviour of droplets in simple shear flow in the presence of a protein emulsifier. *Colloids Surfaces A*, 125:189–200, 1997.

[2] Y. T. Hu, D. J. Pine, and L. G. Leal. Drop deformation, breakup, and coalescence with compatibilizer. *Phys. Fluids*, 12:484–489, 2000.

[3] S. Velankar, P.V Pyuvede, J. Mewis, and P. Moldenaers. Effect of compatibilization on the breakup of polymeric drops in shear flow. *J. Rheol.*, 45:1007–1019, 2001.

[4] H. K. Jeon and C. W. Macosko. Visualization of block copolymer distribution on a sheared drop. *Polymer*, 44:5381–5386, 2003.

[5] Y. T. Hu and A. Lips. Estimating surfactant surface coverage and decomposing its effect on drop deformation. *PRL*, 91:044501, 2003.

[6] J. M. Rallison. The deformation of small viscous drops and bubbles in shear flows. *Annu. Rev. Fluid Mech.*, 16:45–66, 1984.

[7] D. Barthès-Biesel and A. Acrivos. Deformation and burst of a liquid droplet freely suspended in a linear shear field. *J. Fluid Mech.*, 61:1–21, 1973.

[8] H. A. Stone and L. G. Leal. The effects of surfactants on drop deformation and breakup. *J. Fluid Mech.*, 220:161–186, 1990.

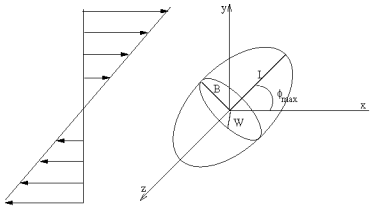

Figure 1: Schematic representation of drop deformation in a linear flow. Drop length, breadth and width are defined as $L = r\left(\frac{\pi}{2}, \phi_{\max}\right)$, $B = r\left(\frac{\pi}{2}, \phi_{\min}\right)$, $W = r\left(\theta_{\max}, 0\right)$, respectively, where $r\left(\theta, \phi\right)$ defines the position of the interface.

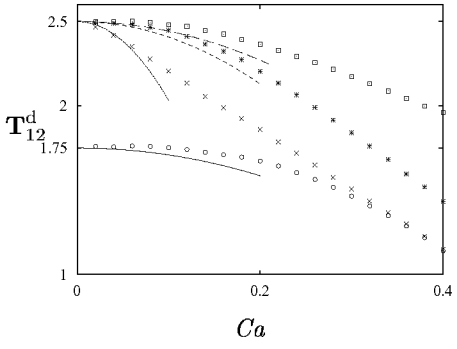

Figure 2: Dependence of the shear viscosity of an emulsion of surfactant-covered drops on flow strength $\kappa-1$ at different elasticities of the surfactant monolayer: surfactant-free drop (circles, solid line), $E = 0.25$ (crosses, dotted line), $E = 1$ (stars, dashed line), $E = 4$ (squares, dot-dashed line). The points are data from BIM numerical simulation. The lines represent the third-order small deformation theory (8).

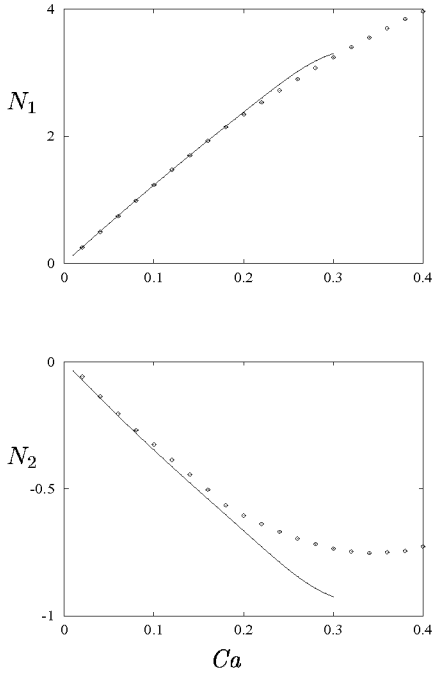

Figure 3: Normal stress differences for an emulsion of deformable surfactant-covered drops with $E = 1$. Points are results from BIM numerical simulation. The line is the prediction from the small deformation theory.

ELUXYL™ Twin Raffinate Technology

Luc WOLFF and Philibert LEFLAIVE

Institut Français du Pétrole
IFP-Lyon
BP 3
69390 Vernaison
FRANCE

e-mail : luc.wolff@ifp.fr or philibert.leflaive@ifp.fr

Keywords : Simulated Moving Bed, Eluxyl™, Twin Raffinate, xylenes

Prepared for presentation at the 2004 Annual Meeting, Austin, November 7-12
Session : Industrial Liquid Phase Adsorption

Introduction

Simulated moving bed (SMB) has been extensively used for forty years as the preferred technology for liquid adsorptive industrial separation. Among the different applications of this technology, the paraxylene recovery from C_8-aromatic cut is the far most known. AXENS*IFP group technology* ELUXYL™ process is one recent and efficient technology for paraxylene production which has been developed by IFP (Institut Français du Pétrole) and commercialized by AXENS (Ash et al., 1994), (Hotier et al., 2000), (Hotier and Méthivier, 2002).

In its conventional operation, the SMB process is characterized by two inlets, desorbent and feed injections, and two outlets, extract and raffinate withdrawals. These four streams delimit four zones which can be defined as follows : zone 1 is located between desorbent and extract streams, zone 2 between extract and feed streams, zone 3 between feed and raffinate streams and finally zone 4 between raffinate and desorbent streams. Taking into account the target of coproducing several products with the same unit, SMB process may be operated with an additional outlet (second raffinate or second extract) leading to one additional zone.

The objective of this work is to present the results obtained during the development of the ELUXYL™ Twin Raffinate process for the coproduction of PX and MX/OX mixture. In a first part, breakthrough experiments obtained for a xylene mixture with a particular adsorbent / desorbent couple are presented. It is shown that the selectivities of the different components are as follows : PX > EB > MX≈OX. Then, in a second part, results obtained on a SMB pilot plant operated with a second raffinate are stated. It is shown that by adjusting the ratio of the two raffinates

flowrates, it is possible to produce a mixture of meta- and orthoxylene isomers almost free of paraxylene and ethylbenzene in the second raffinate, with high purity PX being still recovered in the extract. In a last part, features about how to integrate this ELXUYL Twin Raffinate process in two process schemes to coproduce pure PX and either pure MX or OX are given.

Breakthrough experiments

When one looks at the development of an adsorption separation process, breakthrough experiments are an important part of the R&D work that has to be carried out. In fact, this type of experiments, with a suitable methodology of exploitation, allows to evaluate both thermodynamic and mass transfer data of the system.

Figure 1 displays a typical view of a breakthrough apparatus. This experimental system includes the following devices :

- two distribution networks (tank + pump + switch valve) : one for feed and one for desorbent. This enables to carry out breakthrough experiments (desorbent replaced by feed in the adsorbent column) or reverse breakthrough experiments (feed replaced by desorbent in the adsorbent column)
- one air bath where the adsorbent column is placed
- one cooler at the outlet of the heating system
- one fraction collector for chromatographic analysis

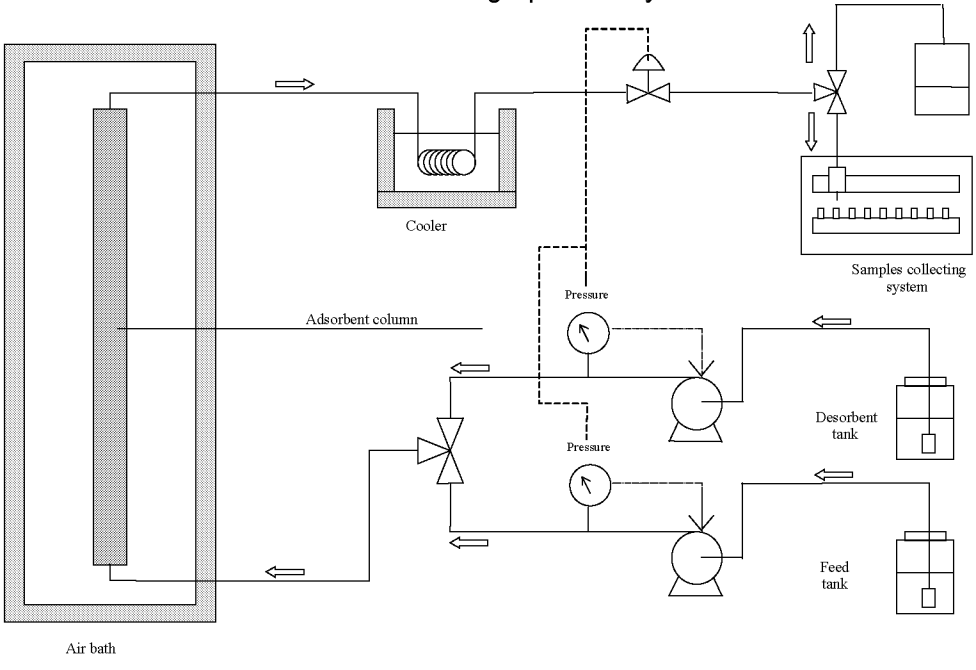

Figure 1 : Schematic view of an experimental breakthrough apparatus.

For a xylene mixture, which is our case of interest, we carried out a set of experimental breakthrough tests with different adsorbent / desorbent couples. One of them shows a particular behavior regarding the selectivities for the different components. These selectivities are in the following order : PX > EB > MX≈OX as it is

shown on figures 2.a and 2.b : indeed, it can be seen that EB breakthrough curve is intermediate between PX and MX curves.

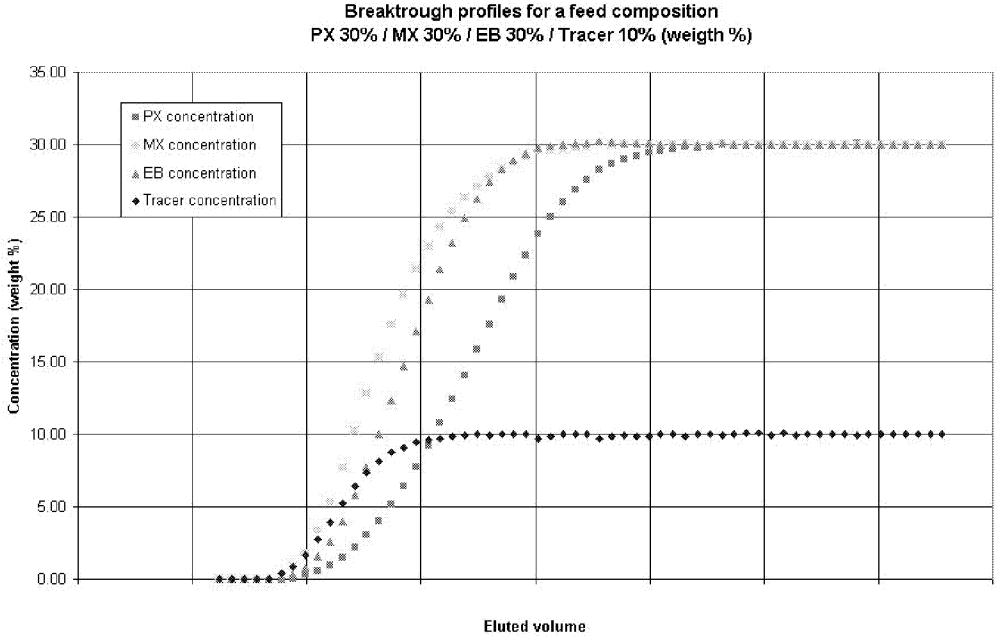

Figure 2.a : Breakthrough profiles for a xylene mixture of following mass composition : PX 30% / MX 30% / EB 30% / Tracer 10%.

An non-adsorbed tracer is used for non-selective volume evaluation. We observed that OX has the same behavior as MX regarding the selectivity. Therefore, OX was not specifically considered in our experiments.

Thermodynamic and mass transfer parameters were extracted from the set of experimental data (breakthrough + reverse breakthrough profiles). Those parameters were then implemented in a SMB process model to determine the operating parameters needed for the Twin Raffinate operation. This is going to be detailed in the next part.

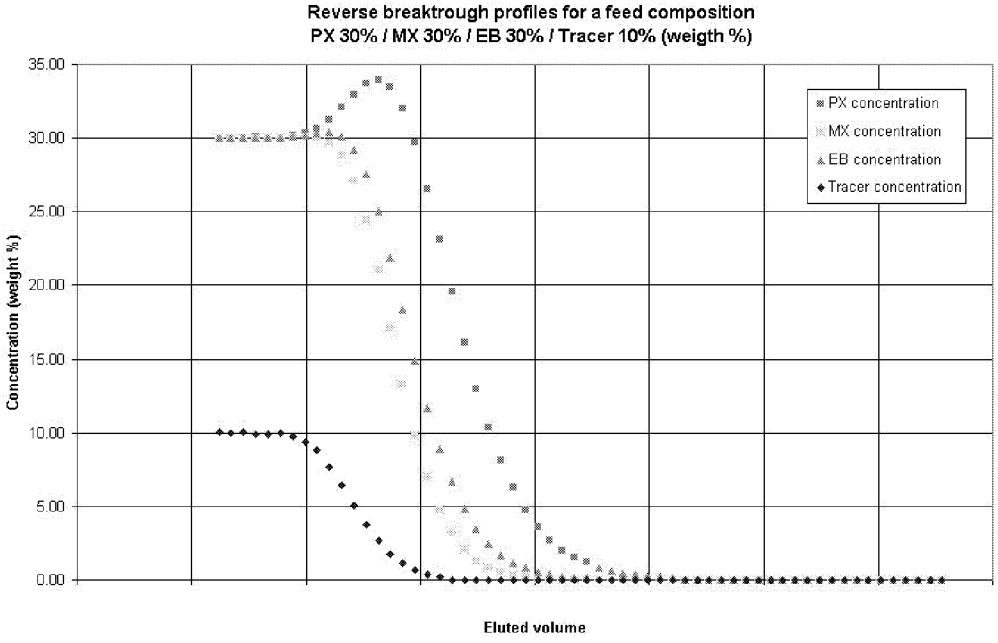

Figure 2.b : Reverse breakthrough profiles for a xylene mixture of following mass composition : PX 30% / MX 30% / EB 30% / Tracer 10%.

Simulation study, pilot plant tests and results analysis

Brief description of SMB Single and Twin Raffinate features

Before investigating the results obtained, we just remind a brief description of SMB process and we focus more particularly on the main features of the Twin Raffinate mode. In the case of paraxylene (PX) production, the conventional four zones SMB process allows to separate PX, which is recovered in the extract, from metaxylene (MX), orthoxylene (OX) and ethylbenzene (EB) which are withdrawn in the raffinate. More particularly, by adequately adjusting liquid flowrates in the different zones along with switching time value, the SMB process allows to produce PX with high purity and recovery. Figure 3.a displays a schematic configuration of a SMB Single Raffinate.

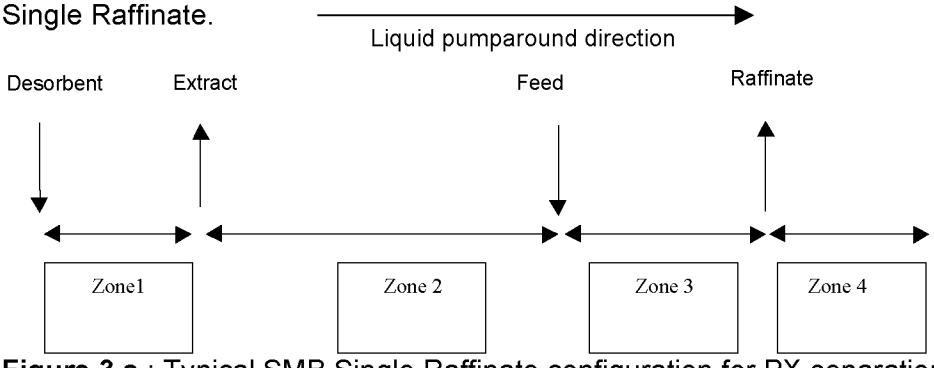

Figure 3.a : Typical SMB Single Raffinate configuration for PX separation.

As presented above, with a particular adsorbent / desorbent couple, the selectivity of the different components are as follows : PX > EB > MX≈OX. Then, considering the case of a SMB operated with a second raffinate, the so-called Twin Raffinate mode, former zone 3 (located between the feed and the raffinate) is subdivided into two zones : zone 3A (from the feed to the first raffinate) and zone 3B (from the first raffinate to the second raffinate). By adequatly adjusting the flowrate in zone 3B (for a given switching time), MX/OX mixture can be separated from EB. As shown below, the operating parameter for adjusting zone 3B flowrate is the ratio of raffinates flowrates R2/R1. Figure 3.b displays a schematic configuration of a SMB Twin Raffinate.

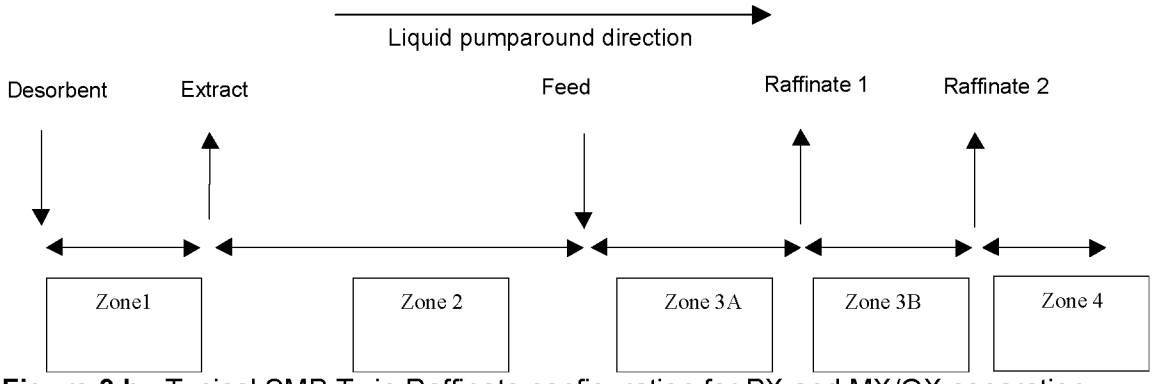

Figure 3.b : Typical SMB Twin Raffinate configuration for PX and MX/OX separation.

Simulation studies

Considering existing commercial PX units, the simulations and the experimentations shown below were carried out in order to evaluate the feasability of adding an MX or an MX+OX coproduction in a limited revamp leading to keep 24 beds. For a new unit a different number of beds would be considered.

Simulations showed that the difference of selectivity between EB and MX/OX mixture allows a separation provided that correct configuration (number of beds) and flowrate of zone 3B are chosen. Different configurations were tested and flowrates were tuned to get a significant separation of MX/OX mixture from EB. Another aim was of course to keep PX purity and recovery equal to that of a conventional four zones SMB. It has been determined that :

- at least 3 beds are needed in zone 3B to get a noticeable separation between EB and MX/OX. Different configurations were tested, the total number of beds being 24, which is the number of beds classically used in a four zones SMB for PX separation. We thus were able to find out the optimum configuration for the Twin Raffinate operation.
- the ratio of flowrates of raffinate 2 to raffinate 1 (R2/R1) has to be in the range [0.4 - 0.7] to get interesting MX and OX purity and recovery.

Taking into account those simulation results, we performed pilot plant tests within the range of operating parameters of interest for coproduction of PX and MX/OX mixture.

Pilot plant tests : results and discussion

A series of pilot tests were carried out in order to validate the simulation studies made earlier. MX/OX purity and recovery that could be reached while maintaining PX purity and recovery at the level of the conventional ELUXYL^{TM} process (purity > 99.8% and recovery > 97%) were evaluated.

On figure 4, a general view of the pilot plant and a detailed view of the on / off valves system for injections and withdrawals are displayed.

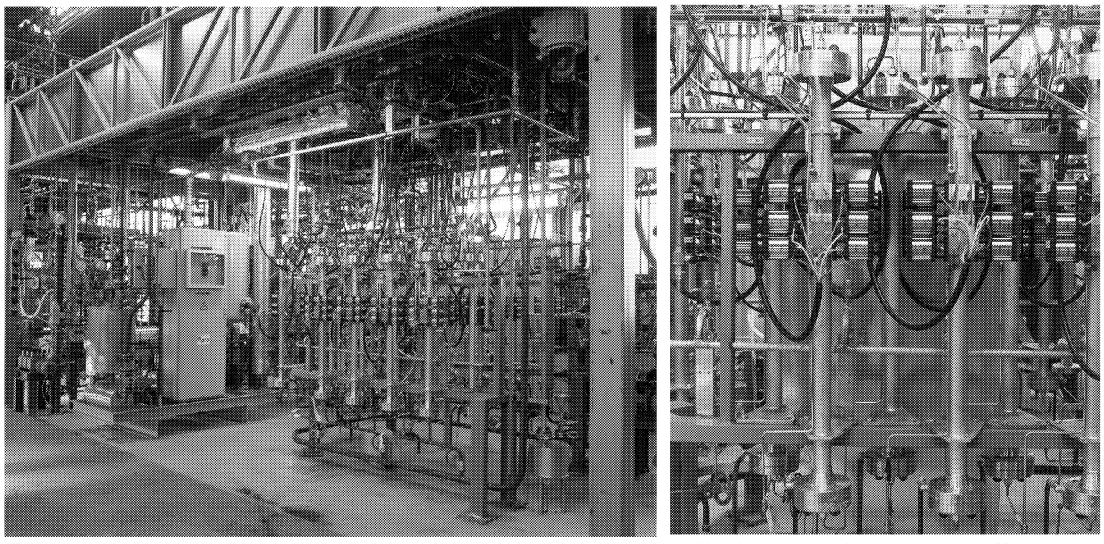

Figure 4 : general view of the pilot plant and a detailed view of the on / off valves system.

Pilot plant was operated in 24 columns mode, with a total volume of adsorbent of 9.1 L. The operating temperature and pressure were respectively 175°C and 10 bars.

On figure 5, the effect of R2/R1 ratio on the experimental concentration profiles within the unit is presented. For the three profiles, in order to physically illustrate what is happening in a Twin Raffinate SMB unit, only R1 and R2 flowrates were varied keeping constant all the other flowrates. For a given R2+R1 total flowrate, R2 was increased (decreasing R1 of the same amount). Doing so, zone 3B flowrate increases so that MX and OX profiles are displaced towards raffinate 2, while EB remains almost completely recovered in raffinate 1. Table 1 gives the detailed operating conditions in terms of flowrates and switching time for the three profiles presented below.

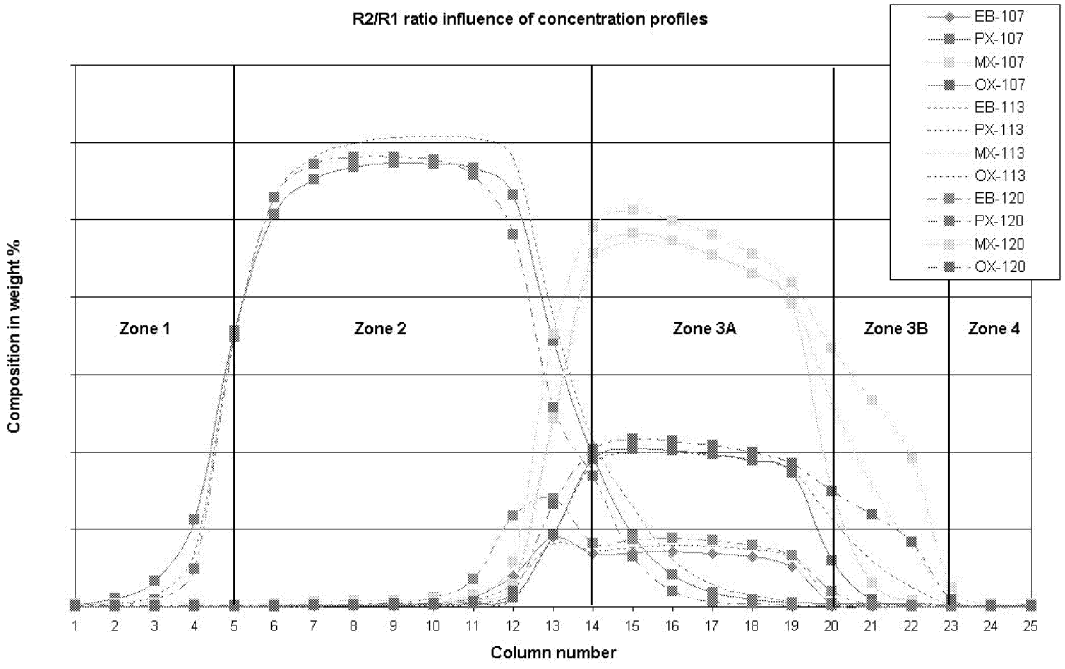

Figure 5 : Influence of R2/R1 operating parameter on the components profiles : profile 107 was obtained with R2/R1 = 0.07, profile 113 was obtained with R2/R1 = 0.21, profile 120 was obtained with R2/R1 = 0.44. All the other operating parameters were kept constants (see table 1 below). The configuration (number of beds per zone) is 4-9-6-3-2.

	Profile 107	Profile 113	Profile 120
Desorbent	91.71	91.73	91.84
Extract	53.37	53.42	53.20
Feed	54.12	54.24	54.24
Raffinate 1	**86.41**	**75.58**	**64.00**
Raffinate 2	**6.05**	**16.97**	**28.88**
Zone 1	274.08	274.02	273.95
Zone 2	220.71	220.60	220.75
Zone 3A	274.83	274.84	274.99
Zone 3B	**188.42**	**199.26**	**210.99**
Zone 4	182.37	182.29	182.11
Switching time	70.80	70.80	70.80

Table 1 : Operating flowrates for the 3 profiles shown on graph 1. All flowrates are in cm^3/min, switching time is in sec.

On figure 6, the evolution of PX, EB and MX+OX concentrations within raffinate 2 as a function of R2/R1 are presented. It can be first seen that the overall C_8-aromatics (i.e. PX+EB+MX+OX) concentration increases with R2/R1 ratio. This is due to a decrease in desorbent concentration in raffinate 2. This decrease can be attributed to the move of the MX and OX, and in a lesser extent EB profiles towards

raffinate 2, which is clearly illustrated on figure 5 where MX and OX concentrations in zone 3B increase.

When R2/R1 becomes greater than 0.4-0.5, there is a radical change of the slope of EB concentration while MX/OX concentration tends to reach a maximal value, thus resulting in a limitation of MX/OX purity. This slope increase is due to the start of EB breakthrough in zone 3B. For values of R2/R1 ratio higher than 0.65, MX/OX purity would start to decrease as :

- EB concentration would still increase until the complete breakthrough of EB profile in raffinate 2.
- MX and OX concentrations would remain almost constant at a value equal to that of the plateau found for the two isomers in zone 3A.

Concerning PX concentration in raffinate 2, it has to be underlined that whatever the value of R2/R1, PX content remains at a relatively constant level ranging in the 0.05-0.1% order of magnitude.

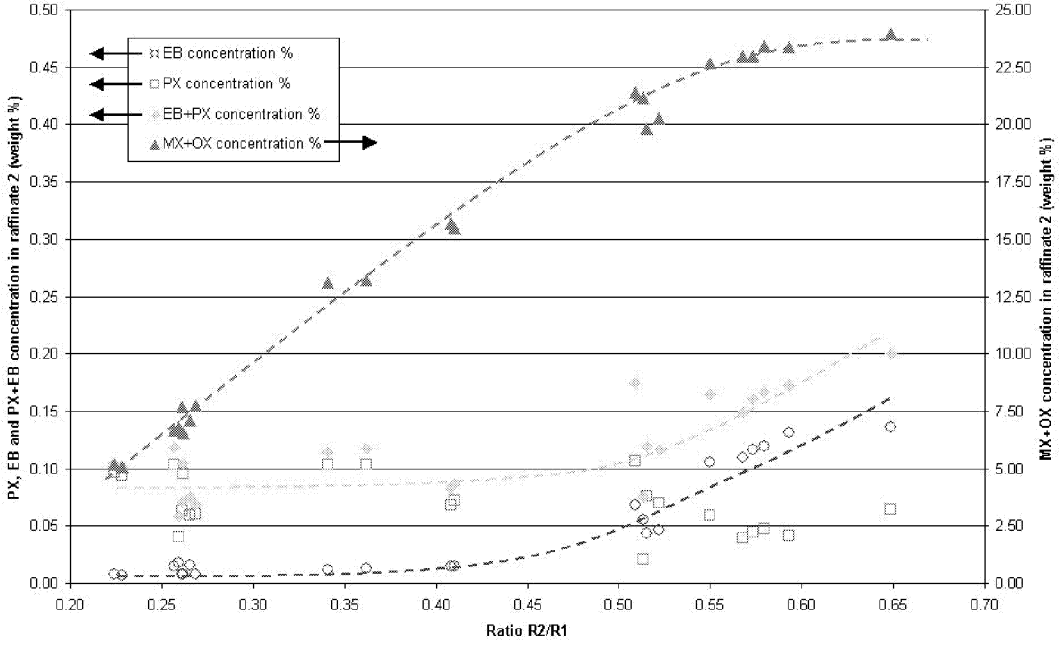

Figure 6 : PX, EB, PX+EB and MX+OX concentrations in raffinate 2 as a function of R2/R1 ratio.

In order to evaluate the performance of the Twin Raffinate ELUXYL™ process for both PX and MX/OX mixture production, the following calculations were used:

- For PX :
  - PX purity $= \dfrac{\%PX_{\text{Ext}}}{\%PX_{\text{Ext}} + \%EB_{\text{Ext}} + \%MX_{\text{Ext}} + \%OX_{\text{Ext}}}$
  - PX recovery $= \dfrac{[\text{PX}]_{\text{Flowrate in Ext}}}{[\text{PX}]_{\text{Flowrate in Feed}}}$

which are the classical formulation for PX purity and recovery.

- For MX/OX :
  - MX/OX purity $= \dfrac{(\%MX + \%OX)_{R2}}{(\%MX + \%OX)_{R2} + \%EB_{R2} + \%PX_{R2}}$
  - MX/OX recovery $= \dfrac{[\mathrm{MX} + \mathrm{OX}]_{\text{Flowrate in R2}}}{[\mathrm{MX} + \mathrm{OX}]_{\text{Flowrate in Feed}}}$

which gives a clear evaluation of both MX/OX recovery and raffinate 2 depletion in PX and EB (other trace components are not taken into account).

MX/OX purity and recovery as a function of R2/R1 ratio are reported in figure 7. It is interesting to notice that for R2/R1 varying from 0.22 to 0.65, MX/OX recovery is linearly increasing from 3.0% to almost 30% while MX/OX purity is increasing from 98.0% up to 99.3-99.4%. For all these runs, PX purity was greater than 99.8% and recovery ranged from 97.0% to 98.0%.

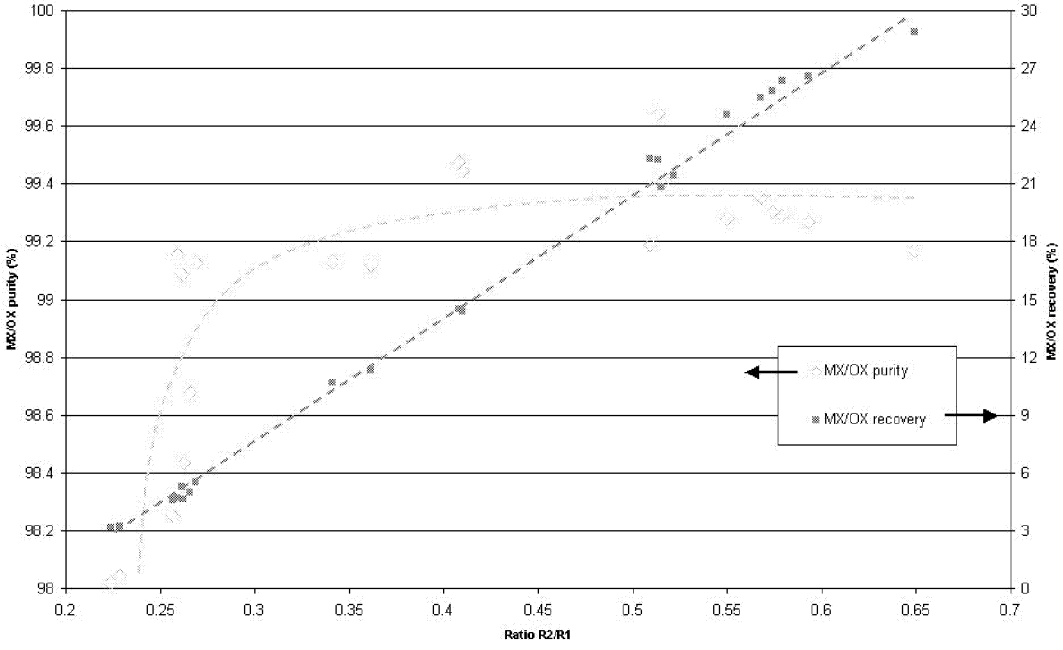

Figure 7 : MX/OX purity and recovery as a function of R2/R1 ratio.

The explanation for the 99.3-99.4% purity plateau that is reached for MX/OX purity for R2/R1 ratios greater than 0.4-0.5 is due to the linear increase of PX+EB concentrations while MX+OX concentration increases and tends to reach a maximal value as illustrated in figure 6.

Pilot plant tests : conclusion

Through the analysis of the pilot plant tests, it has been shown how to operate an ELUXYL™ Twin Raffinate process. More particularly, the evolution of MX/OX purity and recovery in raffinate 2 as a function of the key operating parameter R2/R1 were presented. In terms of performance, PX can be still recovered in extract with high purity and recovery (99.8%+ and 97%+) and a mixture of ortho- and metaxylene can be recovered in the second raffinate. MX/OX purity ranges from 98.0% up to 99.3-99.4%, while the recovery ranges from 3% up to 30% depending on R2/R1 value.

Therefore, the Twin Raffinate technology offers an interesting flexibility for the coproduction of PX and MX/OX mixture. Operation of this Twin Raffinate ELUXYL™ process is not more difficult than the conventional ELUXYL™ process. It is characterized only by the use of an additional operating parameter which is the ratio of the second raffinate flow rate to the first raffinate flow rate. The other regular operating parameters for paraxylene separation are still valid.

In the next part, it is shown how to take advantage of this operation for the coproduction of PX and either pure MX or OX.

Integration of ELUXYL™ Twin Raffinate into two process schemes

Pure MX is the petrochemical intermediate mainly used to produce purified isophtalic acid (PIA) which is then used for the production of modified PET (PolyEthyleneTerephtalate). As the market demand for that form of PET increases, there is an increasing need for producing pure MX.

Concerning OX, it is mainly used to produce phtalic anhydride, a base chemical used in plasticizers and painting industry.

In order to produce pure MX (and possibly pure OX) along with PX, two interesting process schemes were investigated. They are presented in table 2 (Leflaive et al., 2003), (Leflaive et al., 2002). Figures 8.a and 8.b give more details about those two processes.

• Process integration A	• Process integration B
ELUXYL™ Twin Raffinate MX/OX splitter Crystallization unit	ELUXYL™ Twin Raffinate MX SMB unit

Table 2 : General description of process integrations A and B.

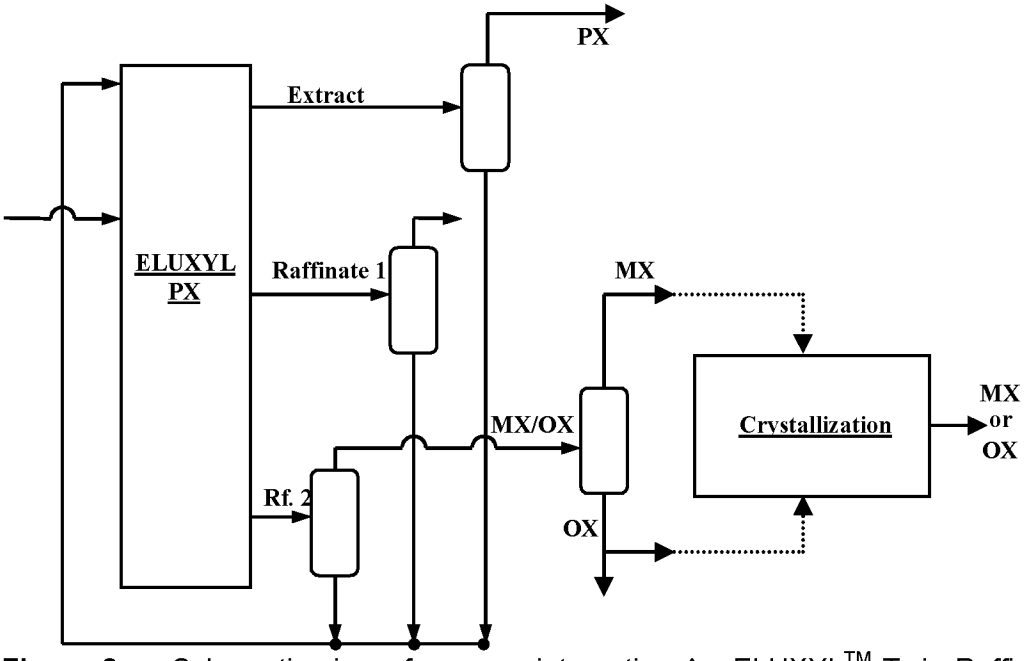

Figure 8.a : Schematic view of process integration A : ELUXYL^{TM} Twin Raffinate + MX/OX splitter + Crystallization.

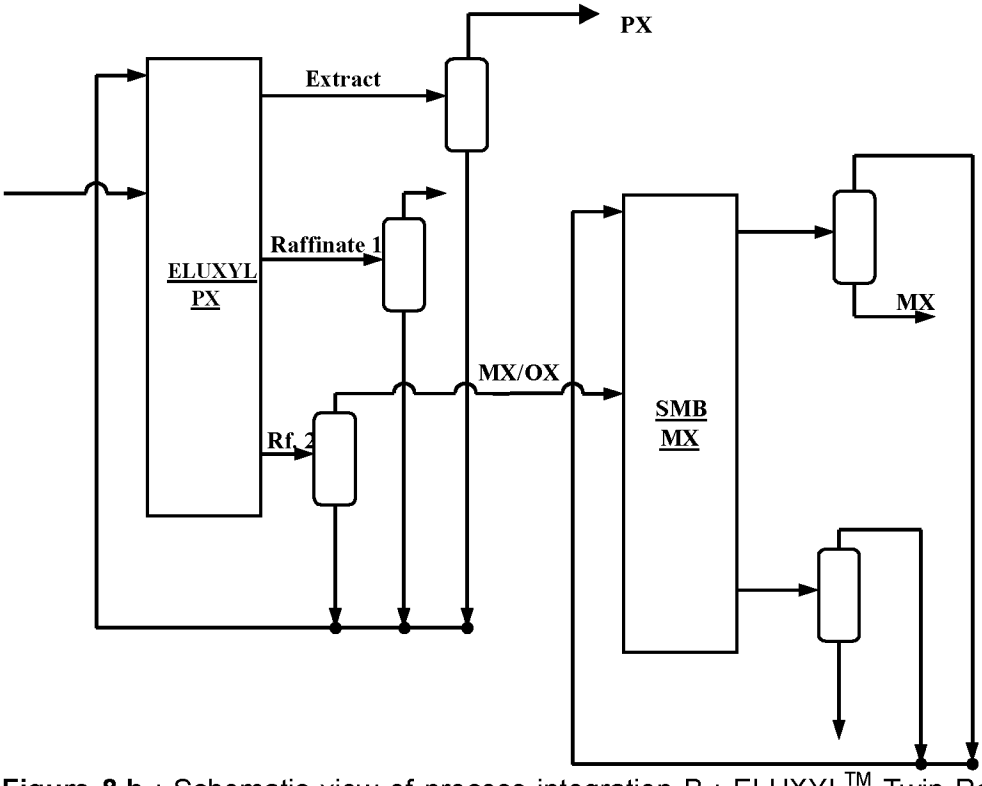

Figure 8.b : Schematic view of process integration B : ELUXYL^{TM} Twin Raffinate + MX SMB unit.

In process integration A, raffinate 2 coming from the ELUXYL^{TM} Twin Raffinate is sent to an MX/OX splitter. Then, either the head or the bottom stream is sent to a crystallizer for production of MX or OX respectively (see figure 8.a). Therefore, the interesting point of this process scheme is the flexibility offered for either producing MX or OX. The main parameter is the composition of the stream sent to the crystallization unit from the splitter. Indeed, depending on which isomer one wants to produce, the composition has to be in the right part of the MX/OX binary solid - liquid equilibrium diagram (see figure 9). One should notice that the very low EB and PX concentrations of raffinate 2 will not affect the binary equilibrium. Therefore for MX crystallization, the composition of the head product should be located in the region delimited by pure MX point, MX/OX binary eutectic point and the liquidus line. For OX crystallization, the composition of the bottom product should be located in the region delimited by pure OX point, MX/OX binary eutectic point and the liquidus line.

Considering process integration B (see figure 8.b), the main aspect is that it is especially dedicated to MX production. Raffinate 2 coming from the ELUXYL^{TM} Twin Raffinate is sent to another SMB unit dedicated to the production of MX at high purity (99.5+%) and high recovery. It can be noted that raffinate 2 is a better feed for the second SMB unit than a conventional single raffinate stream, as it is more concentrated in MX and as it is completely depleted in EB. The use of ELUXYL^{TM} Twin Raffinate technology process integration B allows then to reduce the amount of adsorbent and desorbent needed in MX SMB unit, which leads to important savings in both investment and operational costs for MX coproduction.

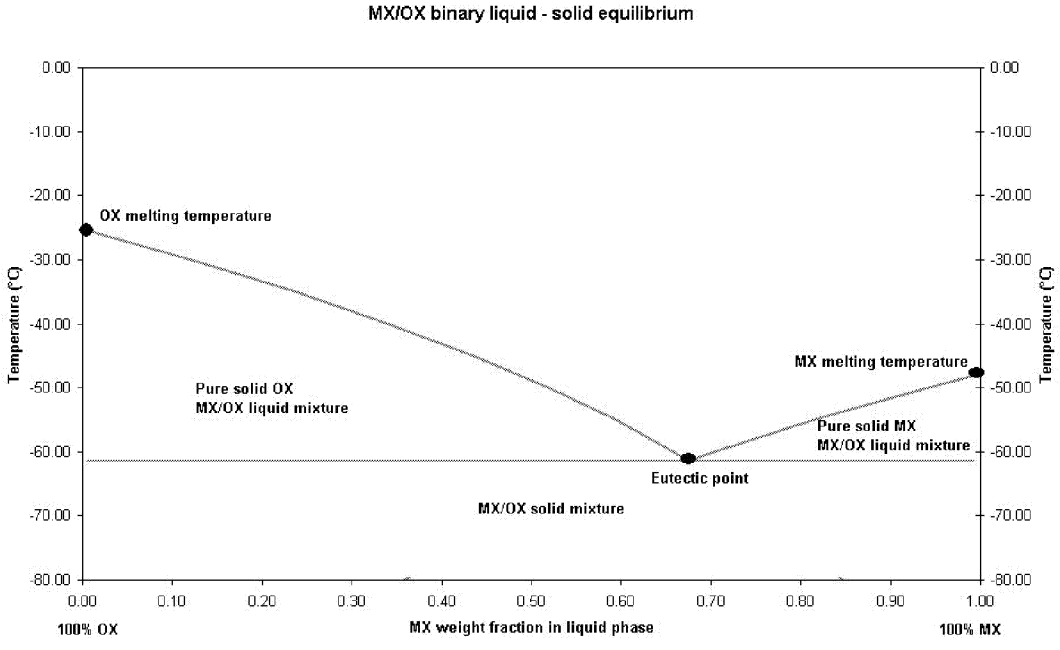

Figure 9 : Binary MX/OX solid - liquid equilibrium diagram.

Conclusion

In this paper, the results of the development of the ELUXYL™ Twin Raffinate technology are presented.

In a first step, breakthrough experiments were carried out, enabling the determination of an interesting adsorbent / desorbent couple. The selected couple exhibits selectivities in the following order : PX > EB > MX≈OX. Simulations showed how this behavior could be smartly used in a Twin Raffinate SMB process and pilot plant tests confirmed that both pure PX and a MX/OX mixture depleted in PX and EB could be obtained in a 24 beds Twin Raffinate SMB unit. In terms of performances, a mixture of MX/OX can be produced with a 99.3-99.4% purity and a recovery ranging from 15% to almost 30% for R2/R1 ranging from 0.4 to 0.6. Those results were obtained at a PX purity and recovery equal to that of a conventional four zones SMB (99.8%+ and 97%+).

Therefore, the Twin Raffinate technology offers an interesting flexibility for the coproduction of PX and MX/OX mixture. Operation of this Twin Raffinate ELUXYL™ process is not more difficult than the conventional ELUXYL™ process. It is characterized only by the use of an additional operating parameter which is the ratio of the second raffinate flow rate to the first raffinate flow rate. The other regular operating parameters for paraxylene separation are still valid. From the engineering point of view, in the ELUXYL™ process, injection and withdrawal of products are operated by a robust independent on-off valves system. Therefore, the conventional ELUXYL™ process would be easily adapted for the withdrawal of a second raffinate by the implementation of a new valves set (24 more valves than a conventional Stand Alone ELUXYL™ process).

Finally, it is presented how it can be taken advantage of the Twin Raffinate operation for the coproduction of PX and either pure MX or OX. Two options are given for the integration of the ELUXYL™ Twin Raffinate. The first one comprises a splitter plus a crystallizer unit that allows coproduction of either MX or OX. The second one is dedicated to MX production using a specific SMB unit for MX separation downstream the ELUXYL™ Twin Raffinate process.

To conclude, ELUXYL™ Twin Raffinate Technology offers an interesting flexibility to coproduce PX and either MX or OX depending on which integration scheme is chosen downstream.

The rapid and successful development of the ELUXYL™ Twin Raffinate technology, clearly shows that IFP and AXENS can rapidly bring both smart solutions to respond to market needs and competitive technological evolutions of the conventional processes.

The efficient and well-tried methodology used, combined with in-depth technical skills of IFP multidisciplinary expert teams, allowed to rapidly come from lab-scale experiments up to industrial applications.

The methodology included :

- Adsorbent studies: Using thermogravimetric, pulse and breakthrough experiments, both thermodynamic and mass transfer data of the adsorbent / desorbent system could be extracted. These experiments, combined with adsorbent formulation specialists know-how, were of great use to get a complete understanding of the physico-chemical phenomena that occur within the adsorbent and in further optimizing the adsorbent / desorbent system design.

- Simulation studies : using different kinds of models, Process Technology Group was able, in a first step, to target the optimal range of operating parameters thus allowing to reduce the pilot plant tests duration and consequently the total duration of process development. In a second step, once pilot plant tests were obtained, the detailed process model was finely tuned on experimental data to help industrial process start-up and operating parameters optimization.
- Pilot plant tests : these experiments could validate simulation results, evaluate performance and optimize operating parameters in industrial conditions (temperature, liquid velocity, industrial adsorbent and feed, …).

The developed methodology, based on the sharing of the knowledge throughout the organization, gives the IFP the ability of resolving both technology and operational issues for the separation technology. This, in turn, brings AXENS a useful support in the analysis, development and implementation of key industrial projects, both revamp and new projects, aiming at a feasible balance between cost-efficiency and downstream equipment safety or product quality.

References

Ash G, Barth K, Hotier G, "ELUXYL - A new paraxylene separation process", Revue de l'Institut Français du Pétrole, 49(5), p 541-549, 1994

Hotier G., MacPherson S., Weber R., Renard P., "Para-xylene production : Integrating modern technological solutions into an existing complex", Proceedings of the 16th World Petroleum Congress, 4, p 173-183, 2000

Hotier G., Méthivier A., "Debottlenecking of Existing Aromatic Production Loop : The Hybrid Eluxyl Process Offers An Attractive Alternative Solution", Proceedings of the AIChE Spring Meeting, paper reference 122d, 2002

Leflaive P., Methivier, A., Hotier, G., "Process for co-producing para-xylene and metaxylene, comprising two separation steps", US20020143223 A1

Leflaive P., Wolff L., Hotier, G., Methivier, A., "Process for co-production of paraxylene, metaxylene and/or orthoxylene", US20030069461A1

Soil Biotechnology Process Simulation using Computational Fluid Dynamics

Umesh Yeole[1], Pattanaik B. R.[2] and Shankar H. S.[3*]
Department of Chemical Engineering, Indian Institute of Technology Bombay,
Powai, Mumbai-400076, India. Fax: 091-22-5723480 / 5726895
E-mail: 1. - yeoleup@iitb.ac.in 2. - biblab65@yahoo.com 3. - hss@che.iitb.ac.in

Abstract:

Soil biotechnology (SBT)is a system for water renovation which makes use of a formulated media with culture of soil micro and macro-organisms to process water and wastewater. The process gives advantage in terms of applicability for very small to large scale; natural aeration, no moving parts except pumps, no sludge, no odor and all green environment. Computational Fluid Dynamics (CFD) is used to study the hydrodynamics as well as rate limiting features of the system. Simulations are performed for different configurations of the bioreactor and the results are compared with laboratory and field experimental data. It is shown that this CFD model can be used to predict behaviour of the process.
Keywords: Soil-bioreactor, wastewater renovation, COD removal, soil-column, permeability, large scale bioreactor, CFD.

1 Introduction

Soil Biotechnology (SBT) is a process for processing of organic and oxidisable matter. In this system fundamental chemical reactions of nature viz. respiration, mineral weathering and photosynthesis are integrated and synergised to bring about the process.

As per carbon cycle, water supports four billion ton live carbon while soil and land support 800 billion ton live carbon. Life evolved in water two billion years ago but moved out on to land impelled by the thermodynamic logic - that life longs for itself and evolution is about minimizing energy needs - that it takes roughly 500 kJ/g live carbon per year to support life in water, 26 kJ/g live carbon per year in soil compared to 3 kJ/g live carbon per year on land. But conventional waste processing uses water as medium contrary to the design of carbon cycle. So in SBT, processing is carried out in soil.

In SBT, respiration serves to bring about oxidation of organics and inorganics and therby substantially reduce oxygen demand, mineral weathering serves to regulate the environment to enable these reactions to occur at the desired rates while photosynthesis serves as a bio-indicator of process performance. (Pattanaik et al., 2003). In warm climates the system is open to atmosphere while in very cold climes suitable closures may be needed. If space is a limitation then multi-staged bioreactor system (biotower) can be used.

SBT houses an engineered ecology of formulated media containing selected micro and macro-organisms such as geophagus earthworm *Pheretima elongata*, bioindicator plants. Bioconversion takes place by bacterial processing of organics and inorganics wherein geophagus worms regulate bacterial population. Patents of Pattanaik et al. (2002, 2004) contain details of media, culture and additives. COD, BOD, suspended solids, color, odor, bacteria, coliforms are removed all in a single all green facility open to atmosphere. It is unlike land treatment which is space intensive and unlike constructed wetlands which engages aquatic ecology.

Fig. 1a shows a schematic of the setup for a batch process and Fig 1b shows the schematic of the cross-section of the bioreactor. During passage of fluid over the media, removal of suspended

*Address all correspondence to this author

Table 1: Gross and simplified chemistry of engineered chemical reactions at work during bio-filtration. (Pattanaik et al., 2003b)

Respiration

$(CH_2ON_xP_yS_zK_y)_n + nO_2 + nH_2O$

$= nCO_2 + 2nH_2O$ + Minerals (N, P, S, K) + Energy (2.1)

Photosynthesis

nCO_2 + 2nH_2O + Minerals (N,P, S,K) + Sunlight

$= [CH_2ON_xP_yS_zK_y]_n + nO_2 + nH_2O$ (2.2)

where x = 0.16 - 0.016; y = 0.01 - 0.001; z = 0.02 - 0.002;

Lower values for terrestrial and Higher values for aquatic productions

Nitrogen Fixation

$N_2 + 2H_2O$ + Energy = $NH_3 + O_2$ (in soil) (2.3)

$N_2 + 2H_2O$ + Light = $NH_3 + O_2$ (in water) (2.4)

Acidogenesis

$4C_3H_7O_2NS + 8H_20 = 4CH_3COOH + 4CO_2 + 4NH_3 + 4H_2S + 8H^+ + 8e^-$ (2.5)

Methanogenesis

$8H^+ + 8e^- + 3CH_3COOH + CO_2 = 4CH_4 + 3CO_2 + 2H_2O$ (2.6)

Adding 5 and 6 give overall biomethanation chemistry

$4C_3H_7O_2NS + 6H_20 = CH_3COOH + 6CO_2 + 4CH_4 + 4NH_3 + 4H_2S$ (2.7)

Mineral weathering

$CO_2 + H_2O = HCO_3^- + H^+$ (2.8)

Primary mineral + $CO_2 + H_2O = M^{+n}$ + nHCO_3^- + soil/clay/sand (2.9)

Nitrification

$NH_3 + CO_2 + 1.5O_2$ = Nitrosomonas + $NO_2^- + H_2O + H^+$ (2.10)

$NO_2^- + CO_2 + 0.5O_2$ = Nitrobacter + NO_3^- (2.11)

De-nitrification

$4NO_3^- + 2H_2O$ + energy = $2N_2 + 5O_2 + 4OH^-$ (2.12)

solids takes place by filtration and biological oxidation, dissolved organics by adsorption and/or biological oxidation. Natural aeration serves as the oxygen source. So mass transfer from liquid to solid and biological reactions characterize the device.

Table 1 summarizes the gross and simplified chemistry of the fundamental natural processes engineered in SBT. The soil processes work at mesophilic temperatures (20 45 ^{0}C) wherein the energy of respiration (Eqn. 2.1) is used to derive nutrients such as nitrogen from the environment as per Eqn. 2.3. Bio indicator plants serve to remove excess metabolites via. photosynthesis given by Eqn. 2.2. The chemistry of acidogenesis determines generation of acidity due to decomposition as given by Eqn. 2.5. In addition there could be acidity generation due to nitrification given by Eqn. 2.7 and carbonic acid equilibria as given by Eqn. 2.8. In SBT, formulated mineral additives to regulate pH of the environment is engaged and Eqn. 2.9 gives the chemistry of this weathering reaction; M^{+n} represents the nutrients released from primary minerals and soil/sand/clay are the byproducts of this weathering reaction taking place. Assimilation of nitrogen (assimilatory nitrate removal) and plant uptake as given by Eqn. 2.10, and 2.11 and denitrification as given by Eqn. 2.12 are involved in nitrogen control. These chemical equations serve to quantitate the inputs-outputs from SBT conversion process. (Pattanaik et al., 2003).

Many such plants are operational now for treatment of water containing BOD, COD, ammoniacal nitrogen, coliforms and odor. Field experience suggests the scope to improve the efficiency and to reduce the cost of these plants. Performance enhancement of the bioreactor can be obtained by avoiding flow mal-distribution to improve the contact of fluid with media.

In this work, we present modeling of bioreactor using computational fluid dynamics (CFD) solver Fluent 6.1. Earlier Pattnaik et al. (2003) used a mixed cell model. But performance of large scale devices depend on spatial distribution of fluid. CFD model is advantageous as it solves the conservation equations for total mass, momentum, energy and species mass fraction over the system domain, with specified conditions for space and time.[Ranade, 2002] CFD model for the bioreactor involves only one parameter permeability (or hydraulic conductivity) which could be different in different directions. As shown in the paper permeability could be estimated from RTD data. Thus,

CFD provides a new tool to address large scale simulations. In this work we present CFD model and its validation.

The process uses one or more bioreactors and recycle tanks. CFD takes into account convective and diffusive supply of solute from liquid to solid phase. Darcy's law is used to represent sink term in the momentum balance wherein permeability (alpha) and its variation in the different directions are accounted. Species material balance with appropriate rate equations describe variation of concentrations of the species in the domain of interest. A Langmuir type isotherm is used to describe the equilibria between solid and liquid. The presence of recycle tank introduces a time lag which is accounted by suitable material balance.

The model is simulated for laboratory and field scale devices. Important parameters controlling the process performance are rate constants, residence time of fluid in bioreactor, holding time in recycle tank and permeability of the media. Three cases are considered viz. 30 cm and 1.75 m deep cylindrical beds and commercial facilities.

Comparison of CFD simulations for batch experiments together with known kinetic parameters indicate that CFD model captures the features of the process very well. Comparison of CFD simulations with rates obtained in commercial facilities also show excellent agreement.

In conclusion we show that CFD is a powerful tool if parametrs of the fluid mechanics, biological reactions and transport processes kinetics are available and provides a focus on the parameter values needed for process performance.

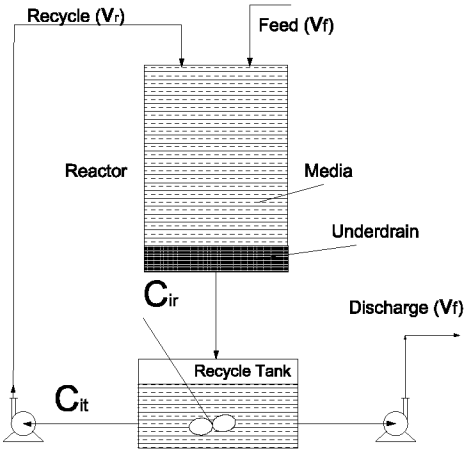

(a) Schematic of experimental setup for biofiltration process. Here, C_{ir} is concentration of species at exit of reactor, C_{it} is concentraion of species in recycle tank

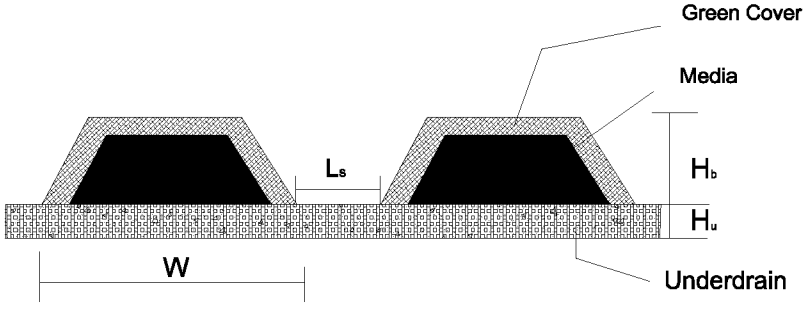

(b) Schematic of cross-section of field SBT bioreactor. Here, W is the width of media strench, H_b is the height of the media, H_u is height of underdrain.

Figure 1: Schematic of SBT Bioreactor

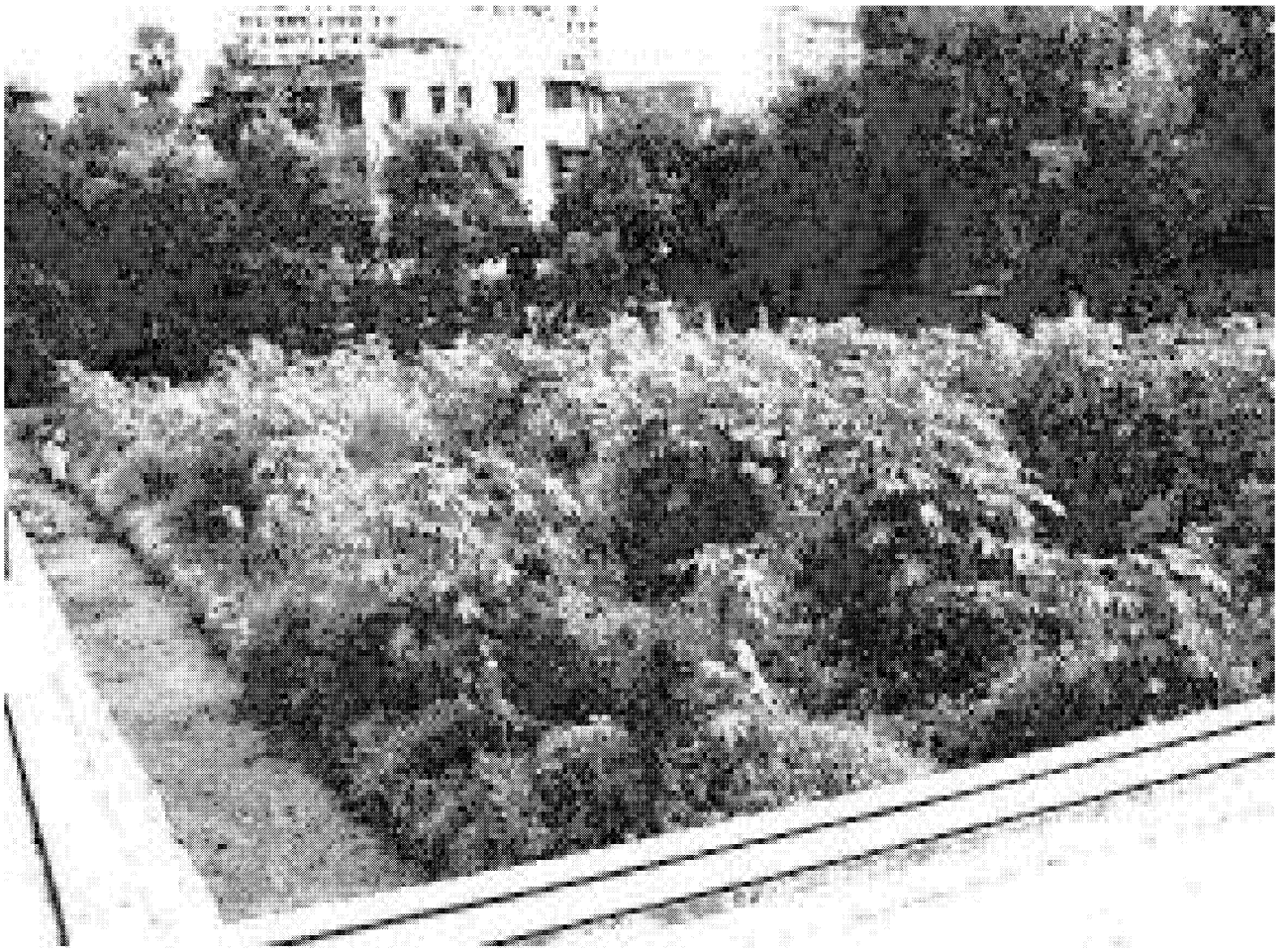

Figure 2: Fuly Commissioned SBT Bioreactor (Bombay Presidency Golf Club, Mumbai.)

Table 2: Specification of the bioreactor media (Pattanaik et al., 2003b)

Item	Details
Underdrain	Gravel - d_p = 25 mm, White Sand d_p = 2 mm,
Media*	Specific gravity- 2.62 BET specifica surface area- 23 m^2/g Cation Exchange capacity- 1.5 g/kg
Soil*	Sand: 67% Silt - 23%, Clay- 10% Specific gravity- 2.66 BET area- 33.6 m^2/g Cation Exchange capacity- 1.5 g/kg
Earthworm	*Phertima elongate*

d_p=Partical diameter. BET: Brunauer, Emmett &Teller (isotherm).
* - Particle size distribution is similar initially, but due to prolonged earthworm movement, it changes with time.

2 Experimental

2.1 Experimental Equipment

Schematic of the 1.6 m deep batch setup is shown in Fig 3. It consists of a reactor containing the media and a recycle tank. The reactor is made of cylindrical aluminum containers, mounted on a metal grid. Sampling ports were provided at every 0.25 m distance. The media in the bioreactor include a bottom layer of gravel (5 cm thick) followed by sand layer (2 cm thick) and finally the active formulated media (1.5 m thick).

A peristaltic pump is used to obtain desired flowrate. A distributor made of rubber tubes with holes ($\simeq$ 1 mm diameter) is used to obtain uniform distribution of the liquid over the surface of media. An overhead tank is used to store the liquid being recirculated from the recycle tank. Centrifugal pump is used to pass the liquid from recycle tank to the overhead tank.

2.2 Bioreactor Media

SBT bioreactors can be grouped in two broad categories - cultured and uncultured; based on the type of media used and the addition of worm culture.
Cultured bioreactor consists of a media housing an engineered ecology of soil, bioindicator plants, soil containing selected micro and macro-organisms such as geophagus earthworms. The media is formulated from variety of materials such as sand, silt, clay, etc and is bioprocesed before filling in the bioreactor. By addition of the earthworm culture, the rates of biological processes are enhanced to bring about the waste processing, as discussed in section 2.1. Bioconversion takes place via. bacterial processing of waste materials where geophagus worms serve as predator to select and regulate the bacterial action. Patents of Pattanaik et al. (2002, 2003a) cover details of culture media and additives used. *Uncultured bioreactors* contains media formulated from sand, silt and clay. (Table 2). No earthworm culture is added. So, the processing is carried out by the activity of selected microorganisms. Details of the media and underdrain used in the SBT bioreactors are given in Table 2. In this work uncultured bed refers to media specifications of Pattanaik et al. (2002, 2003a); cultured bed refers to reactors wherein media culture as specified by Pattanaik (2002, 2003a) is used.

2.3 Experimental Procedure

In a batch experiment, known volume of liquid substrate of interest (viz. sugar solution, glucose solution, sewage or wastewater or drinking water source) is taken in the recycle tank and circulated at a desired flow rate (50-400 L/m^{2}h) using a peristaltic pump. Usually a batch experiment runs

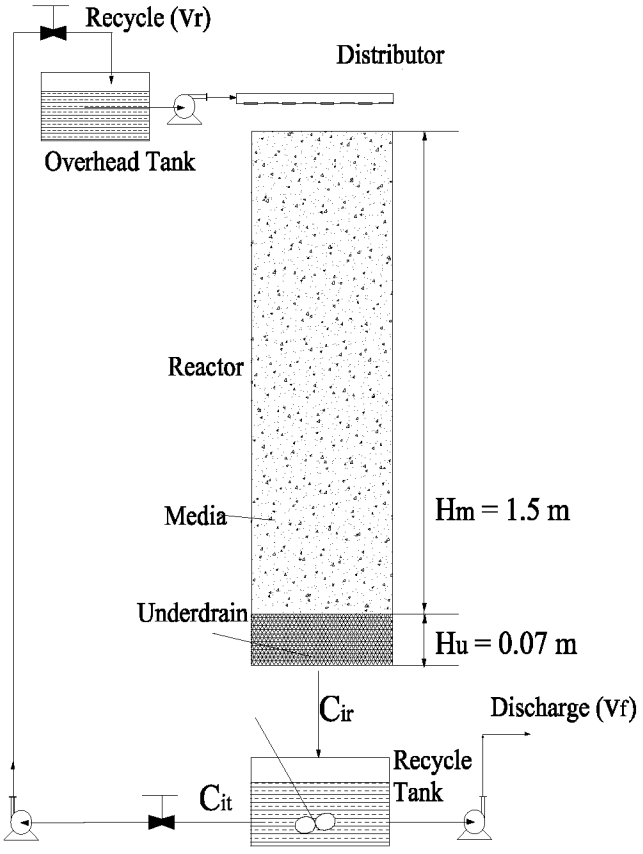

Figure 3: Schematic of Experimental Setup for 1.5 m deep Bioreactor.

for 4-6 hours and during this contacting time, solid liquid equilibrates. Sampling is done from the reactor exit and the recycle tank.

After a batch run, the bed is allowed to regenerate for about 16 h. During regeneration, the organics loaded on the media surface gets degreaded.

Sampling along the height of the bed was not possible, since the flow rates are very low, and hence the contact area between the sampling ports and the flowing fluid stream is very small. So, enough amount of sample could not be collected for analysis.

COD content of the sample was determined by using standard analytical procedure. (APHA et al., 1985). Experiments were performed for different combinations of bed volume, cultured/uncultured media, etc.; for different volumetric feed rate or initial COD content of the fluid. Average substrate removal rate is calculated as,

$$\overline{R_i} = \frac{(S_0 - S_f)V_l}{V_b t_b} \tag{1}$$

where, S_0 is the initial substrate concentration, S_f is final substrate concentration, V_l is volume of the process liquid, V_b is bioreactor volume and t_b is time of the batch run.

3 Computational Model of Soil Bioreactor

Fig 1 shows schematic of the processing of fluid through a porous packed bed bioreactor. To model the soil bioreactor using CFD, a lumped parameter approach is followed, treating the packed bed as anisoropic porous media. Thus, the flow through the bioreactor, liquid to solid mass transfer, and the kinetics of the major biological processes is defined with a series of sub-models such as

1. The momentum loss associated with the packing of the bed particles and the simulation of the anisotropy of the media and underdrain;
2. A surface reactions model to include adsorption, surface reactions and desorption;
3. A mass transfer model to represent the transfer of substrates between the circulating fluid and the bed particles, with consideration of non-equilibrium between the soild and the liquid;
4. Representation of the dispersion effects of the substarates in the fluid due to the presence of the porous particles;
5. A recycle tank model which gives the variation in substrate concentration at reactor inlet due to presence of recycle tank in circulation loop.

These sub-models translate the design/process information regarding the bioreactor into a CFD simulation that completly describes the process. Th model takes into account the convective and diffusive transport of solute and solvent and assumes that removal of substrate follows first order rate equation. For constant density system with low flow velocities, the equations describing conservation of mass and momentum are, (Bird et al., 2002)

$$\frac{\partial \rho}{\partial t} + \bigtriangledown \cdot (\rho \vec{v}) = 0 \tag{2}$$

$$\frac{\partial (\rho \vec{v})}{\partial t} + \bigtriangledown \cdot (\rho \vec{v} \vec{v}) = \vec{F} - \bigtriangledown p + \rho \vec{g} \tag{3}$$

where $\vec{F}$ is the momentum loss term describing the resistance to liquid flow offered by the porous media. For the present system, with low flow velocities through the bioreactor, Darcy's law is followed. (Viottoi et al., 2002).

$$\vec{F} = -\frac{\mu}{\alpha_j} \vec{v} \tag{4}$$

where α_j is the permeability of the medium in direction j. With diffusion flux given by Fick's law, the species conservation equation in terms of local species concentration in the fluid (C_i) is given as,

$$\frac{\partial (C_i)}{\partial t} + \bigtriangledown \cdot (\vec{v} C_i) = -\bigtriangledown \cdot (D_{i,m} \bigtriangledown C_i) + R_i + S_i \tag{5}$$

where, R_i is the rate of degradation of the substrate by biochemical reactions; and S_i is the addition of substrate by liquid-solid mass transfer, and from user defined sources.

During a batch operation, as the water is passed through the bioreactor, organic matter gets loaded on the media surface. This process consists of mass transfer of the substrate from liquid to the media surface followed by uptake; which may be by adsorption, ion-exchange, or by holdup inside the pores. Also, the products of the biochemical reaction such as $NO_3^- - N$, moves back to the liquid.

The substrate consumption rate (R_i) is a function of the rate of the biochemical reactions which mainly take place on the media surface. From Michaelis-Menten kinetics (Belly and Ollis, 1986),

$$R_i = \frac{K_m C_i}{K_{ms} + C_i} \tag{6}$$

For the case of SBT bioreactors, C_i being small, above equation reduces to $R_i = KC_i$, where $K = K_m / K_{ms}$. Also, the term $S_i = k_l a (C_i - C_i^*)$ represents the mass transfer of the substrate from liquid to the media surface. Using an uptake rate constant $k_a = k_l a$; we get $S_i = k_a (C_i - C_i^*)$.

Langmuir type isotherm is used to describe the distribution of species between solid and liquid. So the equilibrium substrate concentration loaded on media is

$$C_i^* = \frac{K_2 q_i}{K_1 - q_i} \tag{7}$$

where, q_i is the substrate loaded on the media surface. Various biochemical reactions taking place in the bioreactor are described. (Table 1). To study the performance of SBT bioractors, main reactions are oxidation of organic matter (Eqn 2.1), nitrification (Eqn 2.10 & 2.11) and de-nitrification (Eqn 2.12). Final forms of the rate processes for the substrates are written as given in Table 3.

Table 3: Rate equations for different substrates in bioreactor

Substrate	**Rate Process**	**Source Term** R_i & S_i
COD	Mass Transfer	(+) $k_{ac}(C_{COD} - C^*_{COD})$
COD	Oxidation	(-) $k_{qc}q_{COD}$
$NH_4^+ - N$	Mass Transfer	(+) $k_{an}(C_{NH_4^+} - C^*_{NH_4^+})$
$NH_4^+ - N$	Nitrification	(-) $k_{qn}q_{NH_4^+}$
$NO_3^- - N$	Nitrification	(+) $k_{qn}q_{NH_4^+}$
Oxygen	Mass Transfer (Aeration)	(+) $k_{a2}(C^*_{o_2} - C_{o_2})$
Oxygen	Oxidation Reactions	(-) $Y_1 k_{qc} q_{COD}$
Oxygen	Nitrification	(-) $Y_2 k_{qn} q_{NH_4^+}$

$$C^*_{COD} = \frac{K_{c2}\ q_{COD}}{(K_{c1} - q_{COD})} \quad \& \quad C^*_{NH_4^+} = \frac{K_{n2}\ q_{NH_4^+}}{(K_{n1} - q_{NH_4^+})}$$

Table 4: Properties and parameter values for CFD simulation of bio-reactor

Description	**Symbol**	**Units**	**Value**	**Source**
Dynamic viscosity of the liquid phase	μ_l	kg/ms	0.001	Viotti et al., 2002
Density of the liquid phase	ρ_l	kg/m^3	998.2	Viotti et al., 2002
Glucose diffusivity in the liquid phase	D_G	m^2/s	6.7x10^{-10}	Viotti et al., 2002
$NH_4^+ - N$ diffusivity in liquid phase	D_{NH_4}	m^2/s	1.7x10^{-10}	Viotti et al., 2002
Oxygen diffusivity in liquid phase	D_{O_2}	m^2/s	2.3x10^{-9}	Viotti et al., 2002
Langmuir isotherm parameters	K_{c1}	g/l	6	Pattanaik, 2000
for COD	K_{c2}	g/L	0.3	
Langmuir isotherm parameters	K_{n1}	g/l	1.55	Pattanaik, 2000
for $NH_4^+ - N$	K_{n2}	g/L	0.1	
COD Uptake rate constant	k_{ac}	h^{-1}	1 - 3	Pattanaik, 2000
$NH_4^+ - N$ Uptake rate constant	k_{an}	h^{-1}	6-11	Pattanaik, 2000
COD degradation rate constant	k_c	h^{-1}	0.04-0.05	Pattanaik, 2000
Nitrification rate constant	k_n	h^{-1}	1.1-1.6	Pattanaik, 2000

Presence of recycle tank in the circulation loop for a batch process introduces time lag for variation of substrate concentration at reactor inlet with time for all the species. This variation of substrate conc. in recycle tank, C_{it} is given as

$$\tau_h \frac{dC_{it}}{dt} = C_{ir}(t) - C_{it}(t) \tag{8}$$

where, $\tau_h = \frac{(V_l - V_d)}{v_r}$ is recycle tank holding time; C_{ir} is the concentration at reactor outlet. concentration in the recycle tank (or reactor inlet).

CFD simulation involves selection of suitable physical models and standard functions defined in FLUENT to represent the system under consideration. For simulation of bioreactor model, the standard models provided in FLUENT solver were not sufficient to describe the system. Hence, user-defined functions (UDF) are used to customize the solver as per requirement to model the bioreactor. UDFs are used to define variation of porosity along the bed dimensions; permeability (viscous resistance) for the media and under-drain; rate terms for the species; and to model the time variation of species concentration entering the bioreactor due to presence of recycle tank.

Two dimensional (2D) grid was generated for different cases of bioreactor configurations as given in Table 5, using *Gambit* and exported to *Fluent*. The model is simulated for different laboratory and field scale devices. Three cases are considered viz. 30 cm and 1.75 m deep cylindrical beds and commercial facilities. Table 4 gives the properties and parameter values used for CFD simulation of bioreactor.

Table 5: Dimensions for bioreactors used in experiments and simulations

Parameter	A	B	C	D
Depth of Media, H_m (m)	0.26	1.5	1.5	0.54
Depth of underdrain, H_u (m)	0.04	0.1	0.3	0.1
Diameter of soil bed, D_b (m)	0.3	0.3	-	0.3
Surface area of soil bed, A_b (m^2)	0.07	0.07	-	0.07
Volume of bed, V_b (m^3)	0.016	0.113	-	0.042

A, B & D - Laboratory beds, C - Commercial facility having tetrahedral cross-section, base = 11.2 m, top surface width=6 m (Fig. 4)

4 Results and Discussion

4.1 Permeability of media

Flow characteristics of soil bed bioreactors differ in axial and radial directions. This results from the presence of micro channels and macro channels formed due to the burrowing movement of the macro-organisms such as earthworms, presence of root zones, etc. which form channels mainly in vertical direction. Permeability values for some materials are given in Table 6.

Simulations were performed for a large scale SBT bioreactor (Table 5-C) with ratio of $\frac{\alpha_a}{\alpha_r} = 1 - 10$. Results are shown in Fig 4. Results with $\frac{\alpha_a}{\alpha_r} = 1$, i.e. for isotropic media, are given in Fig. 4(A) in the form of contours of velocity magnitude. Velocity magnitude remains uniform over a larger portion of the bed cross-section, which is an indication of uniform liquid distribution. As the permeability ratio is increased to $\frac{\alpha_a}{\alpha_r} = 10$, fluid moves mainly in axial direction, as seen from Fig. 4(B) and 4(C). Thus channeling is observed. If the permeability ratio is even higher, say $\frac{\alpha_a}{\alpha_r} = 100$, increased amount of channeling would result in stagnent regions.

Experimental and practical field scale observations indicate that the ratio, $\frac{Pe_r}{Pe_a}$ is roughly equal to the ratio $\frac{\alpha_a}{\alpha_r}$. The results from Baten et al. (2001) for flow through structured packings indicate that the ratio, $\frac{Pe_r}{Pe_a} \simeq 10$. Thus, estimates for the magnitudes of radial permeability can be made, from results available from RTD measurements and from laboratory study of permeability in axial direction. These estimates will be useful for CFD simulations of such systems.

For SBT bioreactors, ratio of axial to radial permeability,(α_a/α_r) from available measurements, is approximately 2. (Table 6). In cultured bioreactors, due to presence of microchannels, the ratio can be in the range of 2-10 or even higher.

Table 6: Permeability values of some Geologic Materials

Material	K_h (m/h)	α (m^2)	Type of Measurement	Reference
Gravel, Coarse	6.25	6.375 x 10^{-7}	R	Todd, 1980
Sand, Medium	0.50	5.1 x 10^{-8}	R	Todd, 1980
Sand, Fine	0.104	1.06 x 10^{-8}	R	Todd, 1980
Clay	8.33e-5	8.5 x 10^{-7}	H	Todd, 1980
Silt	0.0034	3.41 x 10^{-10}	H	Todd, 1980
Media	0.067	6.8 x 10^{-9}	H	Pattanaik, 2000
Media	0.034	3.47 x 10^{-9}	V	Pattanaik, 2000

$\alpha = \frac{\mu}{\rho g} K_h$ where, K_h - Hydraulic Conductivity, α - Permeability, R - Repacked Sample, H - Horizontal Hydraulic Conductivity , V - Vertical Hydraulic Conductivity.

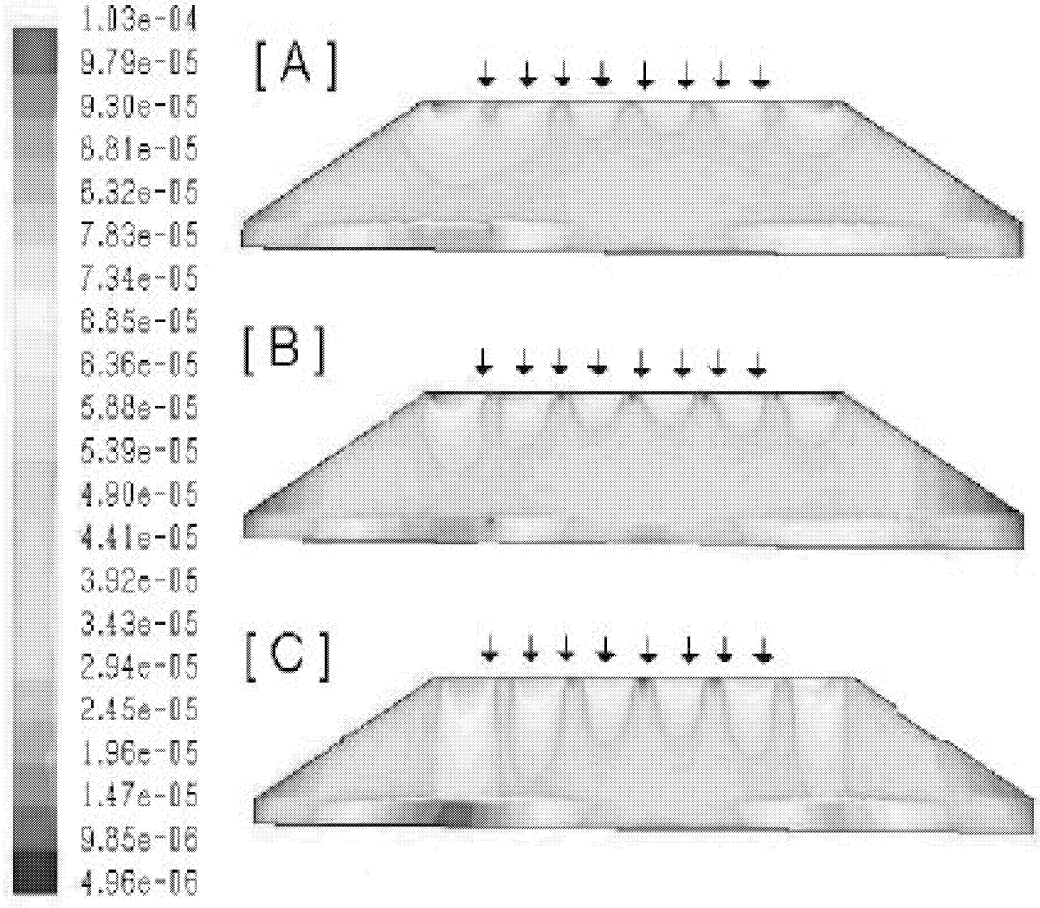

Figure 4: Effect of permeability variation on velocity profile (m/s). Dimensions of the tetrahedral bioreactor crosssection are: base width = 11.2 m, Height of media layer H_m = 1.5m, Height of Underdrain H_u = 0.3 m. v_r = 0.15 m^3/m^2h. (A) Isotropic media, $\alpha_a = \alpha_r = 1.25x10^{-10}m^2$; (B) Anisotropic media, α_a = 5x10^{-10} m^2, α_{rad} = 1.25x10^{-10} m^2; (C) Anisotropic media, α_a = 1.25x$10^{-9}m^2$, α_r = 1.25x10^{-10} m^2

.

4.2 Feed Distribution Arrangement

For bioreactors with large surface area, uniform distribution of the feed over the surface is necessary to obtain good contact of fluid with the media; and hence for better utilization of the reactor. Fig. 5 shows the velocity profiles for simulations with different feed arrangements for a commercial bioreactor (Table 5-C).

In first case; (Fig 5a), fluid enters the bed only from top surface as indicated by the arrows. Here, some regions at the bottom of the bioreactor show zero velocity magnitude. This indicates that fluid has not distributed in entire bed volume.

In second case; (Fig 5b), 70 % water enters from top and 30% water is fed from the slopes of the bed as indicated by arrows. Here, uniform velocity contours are observed over a larger protion of the bed cross-section. This suggest uniform fluid distribution.

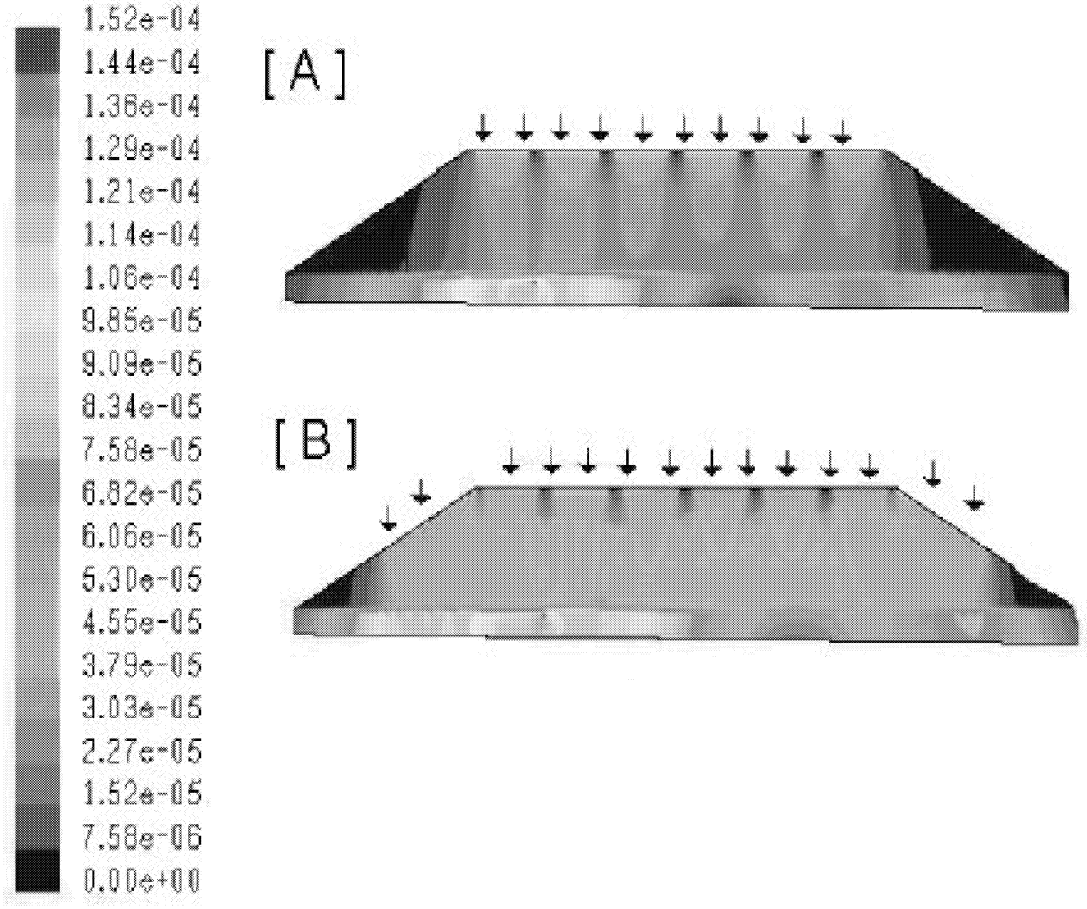

Figure 5: Effect of feed distribution arrangement on velocity profile. Velocity variation in the range 10^{-6}-10^{-4} m/s Superficial flow velocity, v_r=0.15 m^3/m^2h, α_a = 7x$10^{-10}m^2$, α_r = 2x10^{-10} m^2. (A) Water entering from top only. (B) 70 % of water entering from top, 30 % water entering from slopes.

4.3 Flow velocity

Fig. 6 shows the simulation results for substrate removal with different fluid velocities (v_r). As the fluid velocity is increased within the operating range of bioreactors, uptake of COD and ammoniacal-nitrogen increases. These predictions are similar to the trend observed with laboratory and field soil filters. The results are summarized in Table 7.

Uptake of solute during batch process depends on the fluid-solid contact and the residence time of fluid in the bioreactor. With increased superficial fluid velocity, dynamic holdup (V_d) also increases, increasing the fluid solid contact. With this, removal of substrate also increases.

Table 7: CFD Simulation Results for substrate removal: Variation with flow velocity. System paramters : V_b = 113 L, V_l = 25 L, t_b = 6 h. (Fig. 6)

Flow Velocity	**Dynamic Holdup**	**COD Removal**			$NH_4^+ - N$ **Removal**		
v_r (L/m^{2}h)	V_d (L)	Initial (mg/L)	Final (mg/L)	$\overline{R}_{COD}$ (mg/L h)	Initial (mg/L)	Final (mg/L)	$\overline{R}_{NH_4^+-N}$ (mg/L h)
84.86	6	500	225	15.21	20	3.8	1.195
169.7	7	500	120	21.02	20	1.9	1.335
254.5	8.5	500	61	24.28	20	0.6	1.431
339.5	10	500	27	26.16	20	0.25	1.456

Removal Rate, $\overline{R_i} = \frac{(S_0 - S_f)V_l}{V_b t_b}$. t_b = 4 h for all cases.

4.4 Species Transport and Kinetics

Comparison of CFD simulations for batch experiments together with known kinetic parameters indicate that CFD model captures the features of the process very well.

Fig. 7 - 10 shows plots for COD and $NH_4^+ - N$ concentration of fluid with time for cultured bioreactors. For cultured media, COD uptake rate constant, k_{ac} is observed to be 2.5-2.7 h^{-1}; while $NH_4^+ - N$ uptake rate constant, k_{an} is observed to be 10.2-11 h^{-1}. Thus for cultured bed, high rates of substrate removal are obtained. The results are summarised in Table 8. It can be seen that main variables deciding the uptake rates are flow velocities and initial substrate concentrations.

Fig. 11 & 12 shows plots for COD concentration of fluid with time for uncultured bioreactors of 0.3, 0.6 and 1.5 m deep. As the CFD model uses Langmuir isotherm parameters predicted for cultured bioreactors, the model shows deviation from the experimental data. The results are summarised in Table 9.

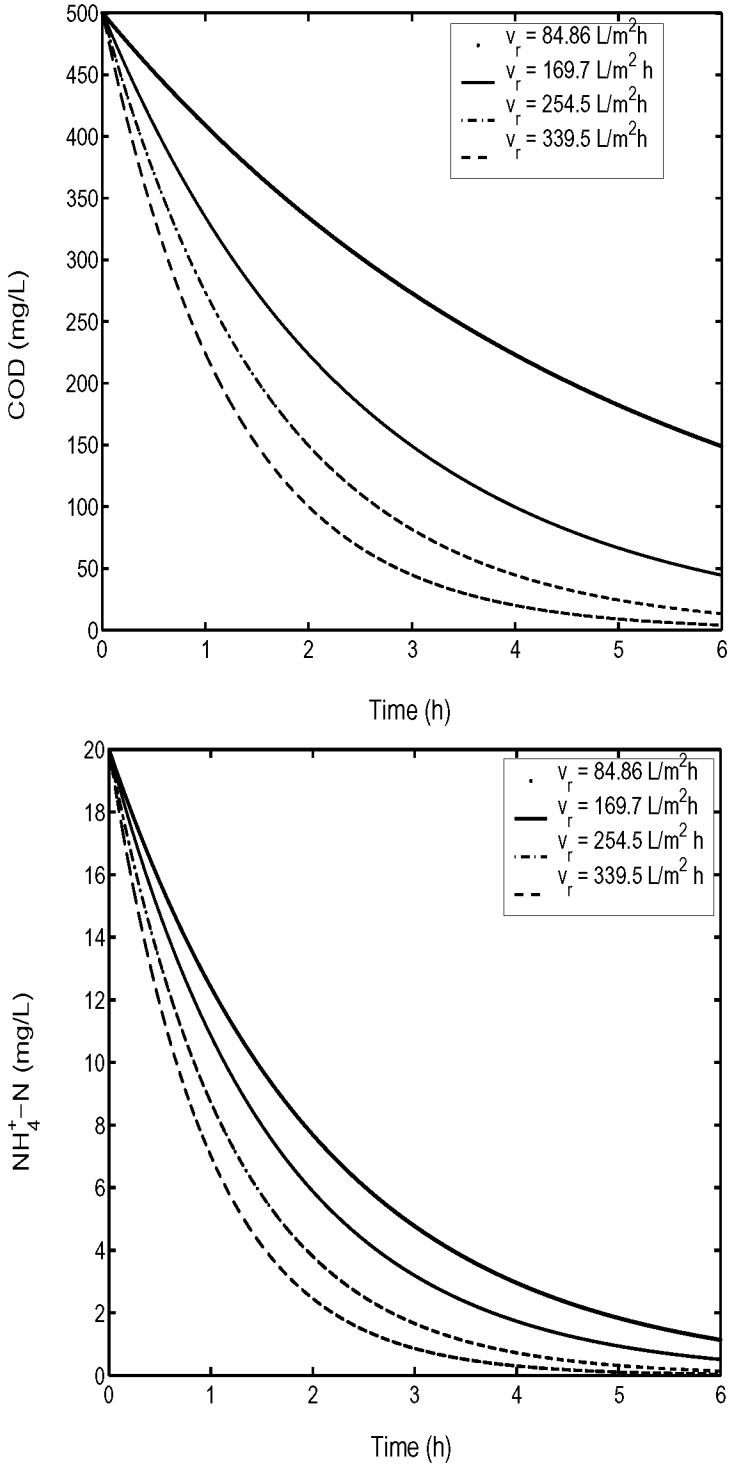

Figure 6: COD and $NH_4^+ - N$ Concentration of fluid: variation with fluid velocity for cultured bioreactors(V_b =113 L, V_l=30 L, k_{ac}=1.5 h^{-1}, k_c=0.05 h^{-1}, k_{an}=11 h^{-1}, k_n=1.5 h^{-1}, α_a = 7x$10^{-10}m^2$, α_r = 2x10^{-10} m^2)

Table 8: Comparison of results of CFD simulation and Experimental data for Cultured Bioreactors

Run No.		BB15	BB16	BB17	BB20
V_b (L)		13	13	13	13
V_l (L)		30	30	30	10
t_b(h)		5.5	5.0	5.0	7
v_r (L/h)		32.4	36	36.6	6
COD Removal					
Experimental	Initial (mg/L)	197.37	227.1	81	212
	Final (mg/L)	51	59	26	88
	$\overline{R}_{COD}$ (mg/Lh)	61.41	75.58	25.38	15.89
CFD Simulation	Initial (mg/L)	197.37	227.1	81	212
	Final (mg/L)	42	51	24	88
	$\overline{R}_{COD}$ (mg/Lh)	65.19	81.28	26.31	15.89
$NH_4^+ - N$ Removal					
Experimental	Initial (mg/L)	5.27	4.02	7.31	9.8
	Final (mg/L)	0.29	0.36	0.68	0.36
	$\overline{R}_{NH_4^+-N}$ (mg/Lh)	2.08	1.69	3.06	1.036
CFD Simulation	Initial (mg/L)	5.27	4.02	7.31	9.8
	Final (mg/L)	0.17	0.1	0.5	0.3
	$\overline{R}_{NH_4^+-N}$ (mg/Lh)	2.14	1.81	3.14	1.044

$A_b = 0.067$ m^2, Average Removal Rate, $\overline{R_i} = \frac{(S_0 - S_f)V_l}{V_b t_b}$.

Table 9: Comparison of results of CFD simulation and Experimental data for Uncultured Bioreactor

Run No.		M1	MB02	MB03	MB04
V_b (L)		16	40	113	113
V_l (L)		15	15	20	27
t_b(h)		4	4	3	4
v_r (L/h)		18	18	15	15
COD Removal					
Experimental	Initial (mg/L)	430	323	501	500
	Final (mg/L)	228	145	143	230
	$\overline{R}_{COD}$ (mg/Lh)	47.34	16.68	21.12	12.66
CFD Simulation	Initial (mg/L)	430	323	501	500
	Final (mg/L)	150	137	30	140
	$\overline{R}_{COD}$ (mg/Lh)	65.625	17.44	27.79	21.5

$A_b = 0.07$ m^2, Average Removal Rate, $\overline{R_i} = \frac{(S_0 - S_f)V_l}{V_b t_b}$.

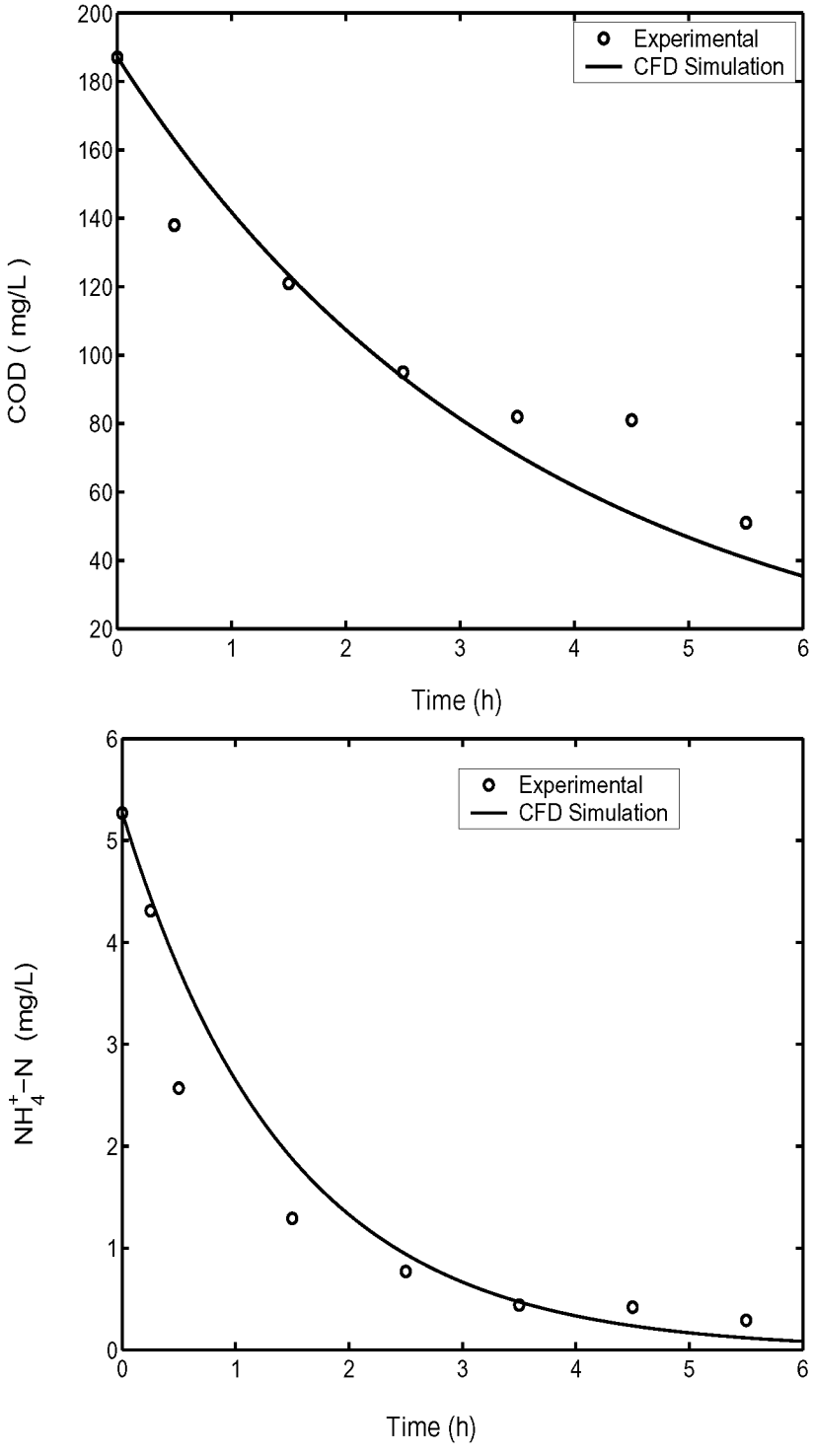

Figure 7: COD and $NH_4^+ - N$ Concentration of fluid with time: comparison with experimental results for cultured bioreactor.(BB15)(V_b =13 L, V_l=30 L, v_r=32.4 L/h, k_{ac}=2.4 h^{-1}, k_c=0.05 h^{-1}, k_{an}=10.4 h^{-1}, k_n=1.5 h^{-1}, α_a = 7x$10^{-10}m^2$, α_r = 2x10^{-10} m^2).

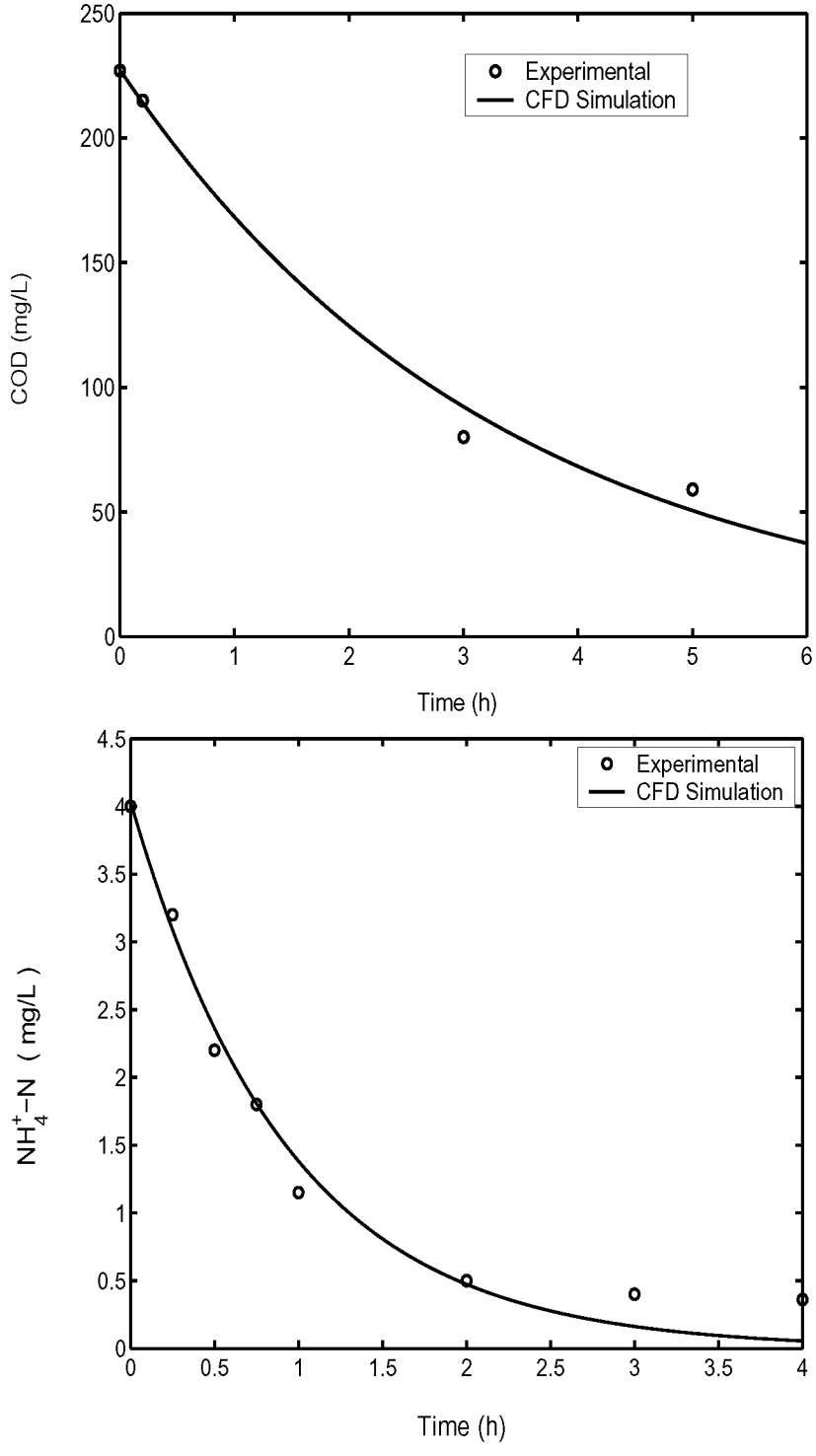

Figure 8: COD and $NH_4^+ - N$ Concentration of fluid with time: comparison with experimental results for cultured bioreactor.(BB16) (V_b =13 L, V_l=30 L, v_r=36 L/h, k_{ac}=2.45 h^{-1}, k_c=0.05 h^{-1}, k_{an}=10.6 h^{-1}, k_n=1.5 h^{-1}, α_a = 7x$10^{-10}m^2$, α_r = 2x10^{-10} m^2.)

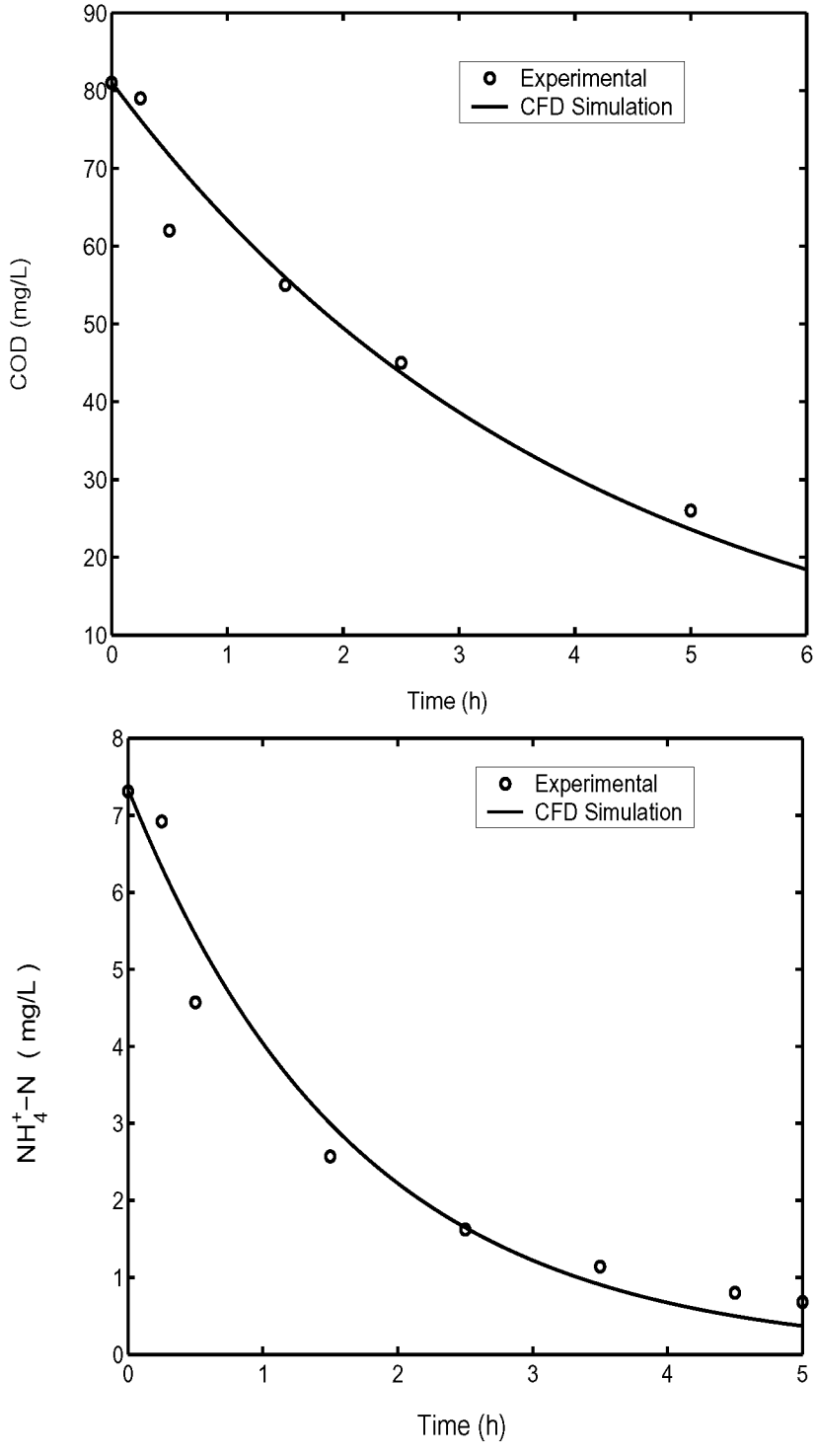

Figure 9: COD and $NH_4^+ - N$ Concentration of fluid with time: comparison with experimental results for cultured bioreactor.(BB17) (V_b = 13 L, V_l = 30 L, v_r = 36 L/h, k_{ac} = 2.45 h^{-1}, k_c = 0.05 h^{-1}, k_{an} = 11 h^{-1}, k_n = 1.5 h^{-1}, α_a = 7x$10^{-10}m^2$, α_r = 2x10^{-10} m^2)

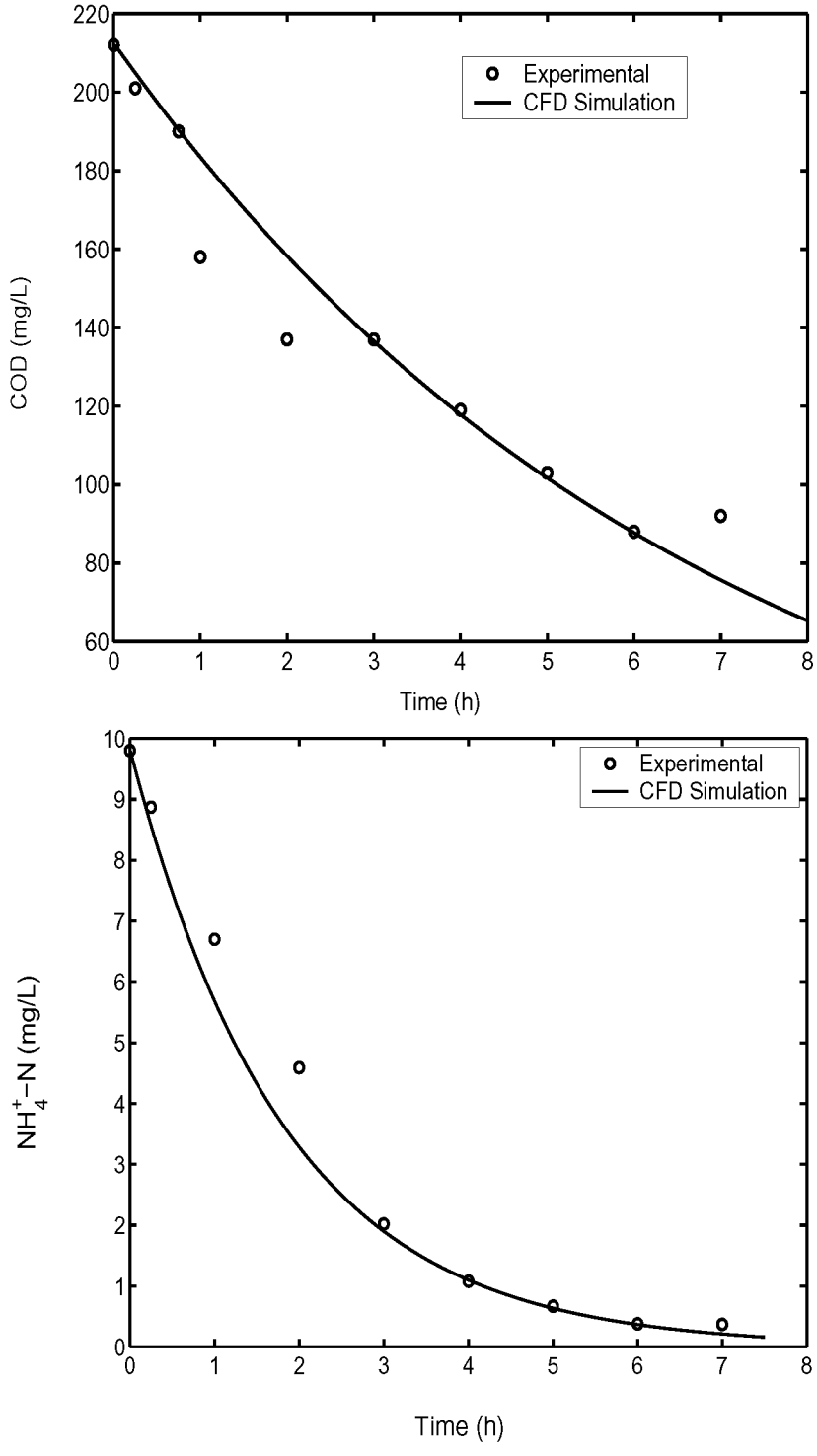

Figure 10: COD and $NH_4^+ - N$ Concentration of fluid with time: comparison with experimental results for cultured bioreactor.(BB20) ($V_b = 13$ L, $V_l = 10$ L, $v_r = 6$ L/h, $k_{ac} = 2.2$ h^{-1}, $k_c = 0.05$ h^{-1}, $k_{an} = 10.4$ h^{-1}, $k_n = 1.26$ h^{-1}, $\alpha_a = 7\text{x}10^{-10} m^2$, $\alpha_r = 2\text{x}10^{-10}$ m^2)

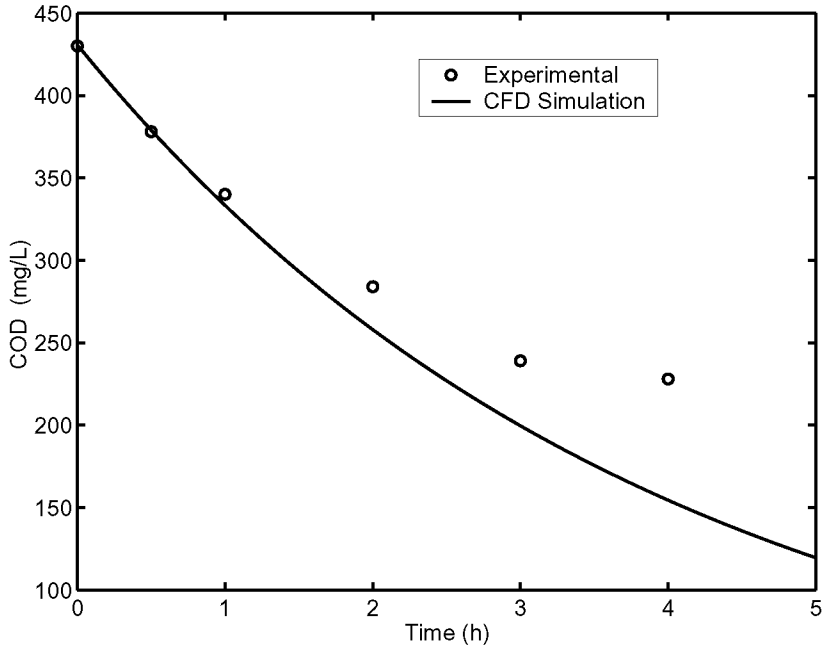

(a) M1

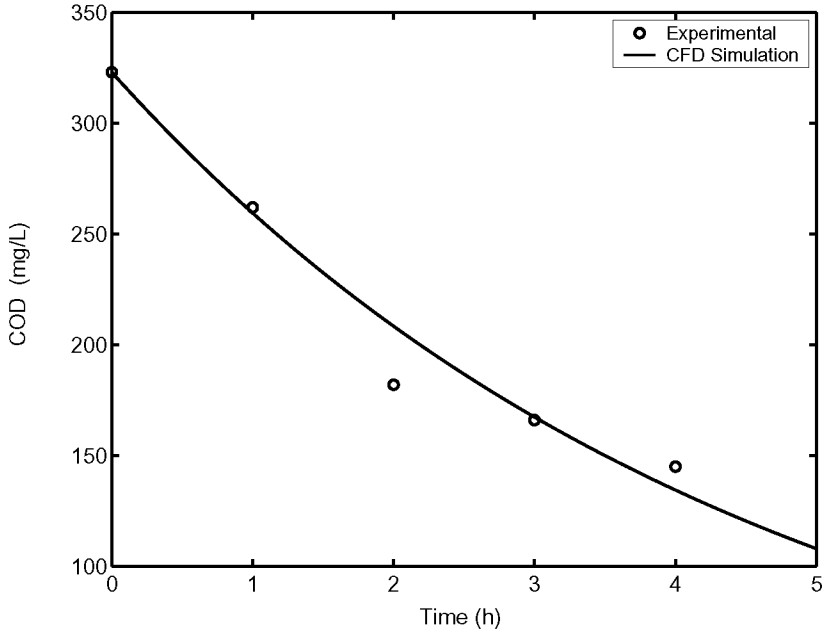

(b) MB02

Figure 11: COD Concentration of dextrose solution with time: comparison with experimental results for 0.3 m and 0.6 m deep uncultured Bioreactors. (A) V_b = 16 L, V_l = 18 L, v_r = 15 L/h, k_{ac} =1.3 h^{-1}, k_c = 0.04 h^{-1}.(B) V_b = 40 L, V_l = 15 L, v_r = 18 L/h, k_{ac} = 0.95 h^{-1}, k_c = 0.04 h^{-1}, α_a = 7x10$^{-11}m^2$, α_r = 2x10^{-11} m^2.

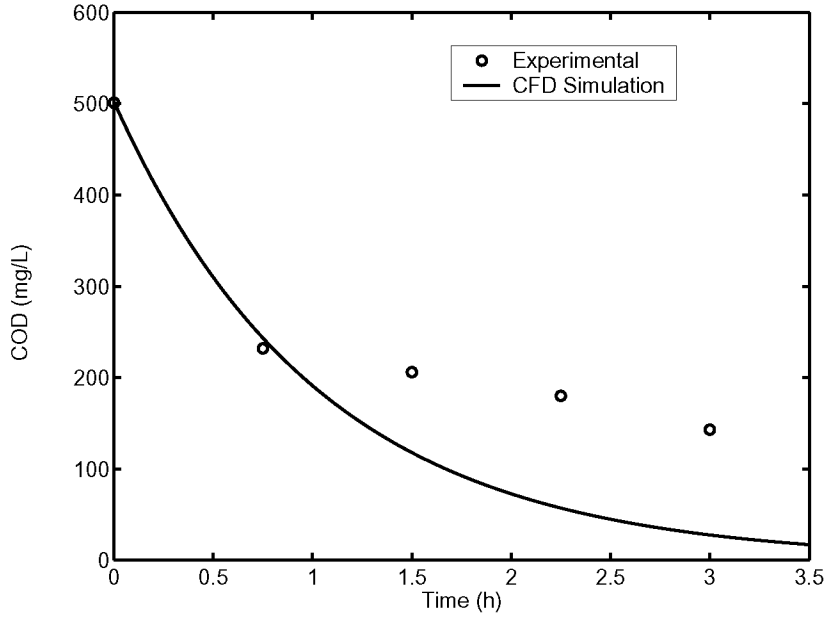

(a) MB03

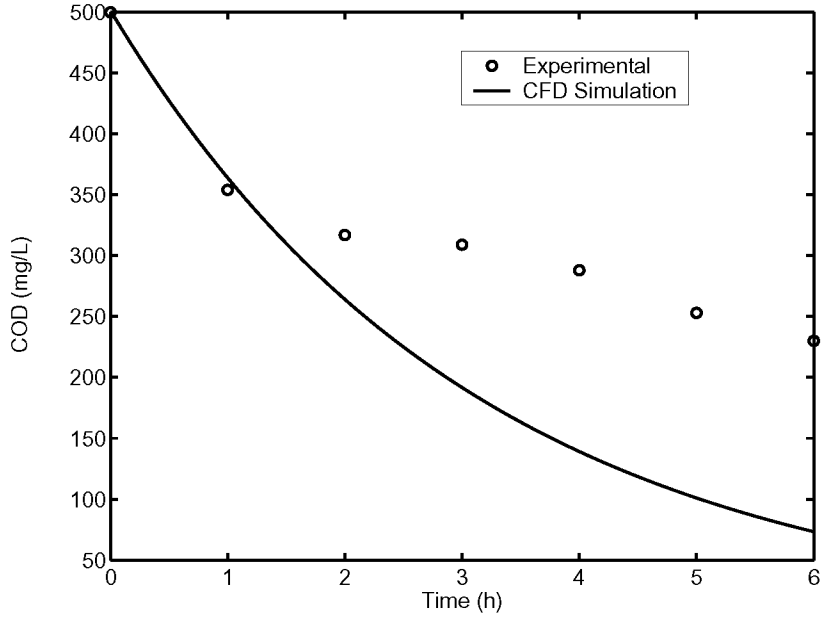

(b) MB04

Figure 12: COD Concentration of dextrose solution with time: comparison with experimental results for 1.6 m deep uncultured bioreactor. (C) V_b = 113 , V_l = 20 L, v_r = 15 L/h, k_{ac} = 0.95 h^{-1}, k_c = 0.04 h^{-1}. (D) V_b = 113 L, V_l = 25 L, v_r = 15 L/h, k_{ac} = 0.8 h^{-1}, k_c=0.04 h^{-1}, α_a = 7x10$^{-11}m^2$, α_r = 2x10^{-11} m^2.

5 Conclusions

The work presented leads to the following conclusions,

1. CFD for modelling flow and reaction through porous SBT bioreactor is a novel way of understanding such bioreactors.

2. CFD model of SBT bioreactor is based on basic conservation principles and is scale dependent. It captures the local effects in the system; reducing the scale-up problems. Thus, performance of large scale systems can be estimated by making use of permeability (α) and rate parameters; determined from simpler laboratory and field scale measurements. So CFD provides a powerful tool for scale-up.

Nomenclature

Symbol	**Interpretation**	**Units**
A_b	Cross sectional area of laboratory bioreactor	m^2
C_i	Molar concentration of species i	$kmol/m^3$
C_{COD}	COD concentration	mg/L
$C_{NO_3^-}$	NO_3^- concentration	mg/L
$C_{NH_4^+}$	NH_4^+ concentration	mg/L
$C^*_{NH_4^+}$	Equilibrium conc. of NH_4^+	g/L
C^*_{COD}	Equilibrium conc. of COD	g/L
C_{ir}	Concentration of species i at reactor outlet	mg/L
C_{it}	Concentration of species i in recycle tank	mg/L
D_b	Diameter of soil bed	m
D_G	Glucose diffusivity in the liquid phase	m^2/s
D_{NH_4}	Ammonia-nitrogen diffusivity in liquid phase	m^2/s
D_{O_2}	Oxygen diffusivity in liquid phase	m^2/s
$D_{i,m}$	Diffusivity of species *'i'* in the mixture	m^2/s
H_b	Total depth of bioreactor	m
H_m	Depth of media	m
H_u	Depth of underdrain	m
K_h	Hydraulic conductivity	m/h
K_{c1}, K_{c2}	Langmuir isotherm parameters for COD	kg/m^3
K_{n1}, K_{n2}	Langmuir isotherm parameters for $NH_4^+ - N$	kg/m^3
k_{ac}	COD Uptake rate constant	h^{-1}
k_{an}	$NH_4^+ - N$ Uptake rate constant	h^{-1}
k_n	Nitrification rate constant	h^{-1}
K_m	Maximum rate coefficient of substrate	kg/kg
K_{ms}	Half saturation constant	kg/m^3
q_{COD}	COD loaded on media surface	kg/m^3 of solid
$q_{NH_4^+}$	$NH_4^+ - N$ loaded on media surface	kg/m^3 of solid
p	Static pressure	pa
Pe	Peclet number (dimensionless)$(=\frac{uL}{D})$	
R_i	Rate equation for species *'i'*	kmol/ m^3 h
t	Time	h
t_b	Batch time	h
V_b	Filter Bed volume	m^3
V_l	Volume of Process liquid	m^3
v_r	Recycle flow rate	m^3/m^2h
Y_1, Y_2	Stoichiometric factors for oxidation of COD and $NH_4^+ - N$ respectively	kg/kg

Greek letters

α	Fraction of macro channel in bed volume	
α	Permeability	m^2
α_a	Axial permeability	m^2
α_r	Radial permeability	m^2
β	Fraction of micro channel in bed volume	
ϵ_d	Dynamic hold up fraction of total bed volume	
ϵ	Porosity of Packed Bed [Soil Bed]	
ρ	Density of liquid	kg/m^3
τ	Space time	h
θ	Dimensionless time	
μ	Viscosity of liquid	kg/m.s
τ_h	Recycle tank holding time	h

Abbreviations

BOD	Biological Oxygen Demand
CFD	Computational Fluid Dynamics
COD	Chemical Oxygen Demand
DO	Dissolved Oxygen
MCM	Mixed Cell Model
RTD	Residence Time Distribution
SBT	Soil Biotechnology
SBR	Soil Bioreactor
TCDM	Two Channel Dispersion Model
UDF	User Defined Function

References

American Public Health Association; Americal Water Works Association; Water Polution Control Federation, 1985, "Standard Methods for Water and Wastewater Examination", 20^{th} ed.; Washington, D. C.

Aris, R., 1965, "Introduction to the Analysis of Chemical Reactors", Prentice-Hall, *pp* 268-269, 297-302.

Baten, J. M., Ellenberger, J. & Krishna, R., 2001, "Radial and Axial dispersion of the liquid phase within a KATAPAK-S structure: experiments vs. CFD Simulations", Chemical Engineering Science, 56, 813-821.

Bailey, E. J. and Ollis, D. F., 1986, "Biochemical Engineering Fundamentals", McGraw-Hill, *pp* 100-106.

Bin, X., Sun D., 2002, "Application of Computational Fluid Dynamics: a Review", Computers and Electronics in Agriculture, 34, 5-24.

Bird, R. B., Steward, W. E., Lightfoot, E. N., 2002, "Transport Phenomena", John Wiley & Sons Inc.

Daga, P., 1992, "A new Biofiltration process for wastewater treatment", M.Tech. Dissertation, Dept. of Chemical Engg., IIT Bombay.

Gorle, N., 1999, "Hydrodynamic and Mass Transfer Studies in Vermiculture", M.Tech. Dissertation, Dept of Chemical Engg., IIT Bombay.

Jiang,Y., 2001, "CFD Modeling of Multiphase Flow Distribution in Catalytic Packed Bed Reactors", Catalysis Today, 66, 209-218.

Khadilkar, M.R., 2001, "Characterization of Macroscale Multiphase Flow Textures in Trickle Beds", Chemical Engineering Science, 56, 1647-1656.

Kinnear, D., 2003, "Computational Fluid Dynamics Modeling of Packed Bed Reactors", http://www.cfdreview.com/art June 15, 2004.

Levenspiel, O., 1972, "Chemical Reaction Engineering", Willey, New York, *pp* 265-272.

Mackenzie, F.T., 1995, "Biogeochemistry", Encyclopedia of Environmental Biology, Academic Press, New York, Vol. 1, *pp* 249-276.

Pattanaik, B. R., 2000, "Processing of Wastewater in Soil Filters", Ph.D. Thesis, Dept of Chemical Engg., IIT Bombay.

Pattanaik, B. R., Bhawalkar, U. S., Shankar, H. S., 2003, "Process of treatment of organic wastes", Patent publication No. US-2004-0065610-A1. 28 April, 2003.

Pattanaik, B. R., Bhawalkar, U. S., Shankar, H. S., 2002, "Process of treatment of organic solid wastes and waste water renovation", Indian Patent application No.383-384/MUM/2002. Mumbai.

Pattanaik, B. R., Bhawalkar, U. S., Kadam, A., Shankar, H. S. & Manglani, J., 2003, "Soil Biotechnology for Waste Water Treatment and Utilization", 13^{th} IWA-ASPAC Conference & Exhibition, Cebu City, Philippines. 13-18 October, 2003. *pp* 181 - 188.

Pattanaik, B. R., Gupta, A., Shankar, H. S., 2004, "Residence time distribution model for soil filter", Water Environment Research, 76(2), 168-174.

Patankar, S. V., 1978, "Numerical Heat Transfer and Fluid Flow", McGraw Hill, *pp* 3-4.

Ranade, V. V., 2002, "Computational flow Modeling for Chemical Reactor Engineering", Academic Press, *pp* 403-420.

Todd, D. K., 1980, "Groundwater Hydrology", Willey, New York. *pp* 71.

Viotti, P., Eramo, B., Boni, M. R., 2002, "Development and calibration of a mathematical model for the simulation of the biofilatration process", Advances in Environmental Research, 7, 11-33.

Zarook, S.M., Shaikh A. A., and Azam, S. M., 1998, "Axial Dispersion in Biofilters", Biochemical Engg. Journal, 1, 77-84.

Calcium Carbonate Decomposition under External Pressure Pulsations

Patil, K., Jain, S., Gandi, R. K., Shankar, H. S.*,
Department of Chemical Engineering
Indian Institute of Technology Bombay, Powai, Mumbai-400076, India
E-mail: hss@che.iitb.ac.in, gandi@iitb.ac.in, kiranp@iitb.ac.in, swatijain@iitb.ac.in

Abstract

In this work effect of pulsating flow on thermal decomposition of a spherical pellet of calcium carbonate is presented. Here we use grain model and solve the unsteady state diffusion reaction equations under external pressure pulsations. The effects on temperature, conversion-time and radial profiles are predicted. It is shown that under pulsating pressure significant improvements in conversion time behaviour can be obtained for diffusion limited conditions. Experimental data are presented to validate the predictions and also pointer applications where such methods might be useful.
Key words: Calcium carbonate, Decomposition, Transport processes in Pulsating flow

1 Introduction

Calcination of limestone, high temperature reactions of cement kilns, smelting of ores, sulfur capture from gases, solid catalysed reactions, drying of grains and industrial products are very large scale examples where heat and mass transfer play crucial role. Limestone calcination technology engages rotary kiln (RK), fluidized beds (FB) and vertical shaft kilns (SK). RK and FB are common for very large scales a million ton/yr plus, while shaft kilns are used for small scales. Limestone decompositions are also carried out in very large quantities in decentralised very small scale may be 2-10 tons per batch using local ores and sea shells. At these scales extent of calcination is an important quality issue. In very large scales all such issues are factored into design by choosing the appropriate scales. In this light the technology of heat and mass transfer need fresh appraisal.

In the normal range of 700-1000°C, the calcination products are calcium oxide and carbondioxide. According to Satterfiled and Feaks (1959) and Ingraham and Marrier (1962) the reaction is controlled by chemical reaction. Narsimhan (1959) postulated that there is no internal temperature gradient and all the heat reaching decomposition plane is used up for the endothermic decomposition. Rao et al., (1989) considered a grain model , solved the unsteady diffusion reaction model for the grain wherein the temperature effects were described by the Prater relationship

$$T_0 - T = \frac{C_{A0} - C_{As}}{h_T/k_g \Delta H} + \frac{C_{As} - C_A}{k_e/D_e \Delta H} \tag{1}$$

where T_0 is bulk temperature, s refers to surface values and the terms in the right are the temperature drop in gas film and in the solid layer; and showed that the pellet conversion temperature-time data could be described adequately by the diffusion reaction model. Murthy (1994) also considered grain model and solved the diffusion reaction equations for simultaneous mass amd heat transfer, also

*Address all correspondence to this author

taking into account the effects of porosity, effective diffusivity and effective thermal conductivity changes in the pellet. The results revealed good agreement with conversion-time data and that the variation in k_e, D_e were not significant to affect the conversion-time predictions.

Introduction of presssure pulsation is an useful way of enhancing the rates of transport processes and has been studied earlier. Increase in rates of reduction of iron ore pellets by hydrogen was found by Ohmi and Usui (1976b) when pulsating conditions were applied. Hamer and Cormack (1978) investigated the utility of periodic external pressures for increasing rates of catalytic reactions in porous catalyst pellets. Sohn and Chaubal (1984) investigated the effects of cycling external pressure for gas solid reactions. Sohn and Aboukheshem (1992) conducted an experimental study on the reduction of nickel oxide by hydrogen. Fraenkel and Nogueira (1998) found enhanced rates of drying when a pulsating field was created by oscillating flow. Ballal (1995) developed a simple model to demonstrate the effect of pressure pulsations on mass transfer through pores. It was found that mass transfer rates can be enhanced when Peclet number and amplitude of pulsing are large.

Maithy(1997) conducted experiments to study the effects of pulsating external pressure at frequency upto 1.25 Hz and A = 0.125 for limestone decomposition in a bed of coal-limestone mixture; Results were promising. Dias et al(2004) conducted experiments on drying of soyabean at A=0.278 atm and frequency of 70 Hz, at 60°C and different moisture content of gas solid. It was found that under pulsating pressure, conversions-time behaviour showed significant improvement for NiO reduction while not effective for drying of soyabean.

In this work (Patil et al, 2004) we focus on the model of the process; compare predictions with experimental data and delineate applicability of the pulsating procedure.

2 Model

At high temperatures (about 900°C), calcium carbonate decomposes to give solid calcium oxide and carbon dioxide gas.

$$\begin{aligned} CaCO_3(s) &\rightarrow CaO(s) + CO_2(g) \quad \Delta H = 178kJ/mol \\ B(s) &\rightarrow C(s) + A(g) \end{aligned}$$

where A is CO_2, B is $CaCO_3$ and C is CaO. Following simplifying assumptions are made in the model:

1. The pellet is made up uniform spherical non-porous grains typically of 6 micron radius (r_g).
2. The grains are uniformly distributed over the pellet volume and the macroscopic structure is unaffected as the reaction progresses
3. There is no temperature graident and concentration gradient inside the grain.
4. The change in temperature and concentration have little effect on the activation energy, effective diffusivity, effective thermal conductivity, heat and mass transfer coefficients and heat of reaction.
5. Permeability of calcium carbonate and calcium oxide is high leading to negligible internal pressure gradient.
6. The pressure pulsations are represented as

$$P = P_0(1 + Asin(2\pi ft)) \tag{2}$$

Mass balance on gas A gives

$$\begin{aligned} \frac{\partial C_A}{\partial t} =& AD_e\{\frac{\partial^2 C_A}{\partial r^2} + p\frac{2}{r}\frac{\partial C_A}{\partial r}\}+ \\ & \frac{1}{p}\frac{dp}{dt}\{\frac{r}{3}\frac{\partial C_A}{\partial r} + C_A\} + r_A \end{aligned} \tag{3}$$

The energy balance equation for pellet is given as

$$\begin{aligned}\rho_p C_p \frac{\partial T}{\partial t} =& K_e\{\frac{\partial^2 T}{\partial r^2} + \frac{2}{r}\frac{\partial T}{\partial r}\} + \frac{C_{pa}}{RT_0}\frac{dp}{dt}\{T \\ &+ \frac{r}{3}\frac{\partial T}{\partial r}\} - (\Delta H) r_A\end{aligned} \tag{4}$$

The balance for solid calcium carbonate grain B gives

$$-\rho_B \frac{\partial r_g}{\partial t} = K_r\{1 - \frac{C_A}{C_E}\}^n \tag{5}$$

The rate of reaction r_A is given by

$$r_A = \frac{3(1-\epsilon_0) r_g^2 K_r\{1 - \frac{C_A}{C_E}\}^n}{r_{g_0}^3}\} \tag{6}$$

C_E is determined by equilibrium partial pressure of CO_2 givenn by Hill and Winter (1956) as

$$log_{10} p_E = -\frac{8792.3}{T} + 10.4022 \tag{7}$$

The initial and boundary conditions for the pellet are

$$C_A = C_{E0} \quad \forall r \text{ at t=0} \tag{8}$$

$$T = T_0 \quad \forall r \text{ at t=0} \tag{9}$$

$$r_g = r_{g_0} \quad \forall r \text{ at t=0} \tag{10}$$

$$\frac{\partial C_A}{\partial r}|_{r=0} = 0 \qquad \text{at t} \geq 0 \tag{11}$$

$$\frac{\partial T}{\partial r}|_{r=0} = 0 \qquad \text{at t} \geq 0 \tag{12}$$

$$-D_e \frac{\partial C_A}{\partial r}|_{r=r_0} = k_g(C_{As} - C_{A_0}) \text{ at t>0} \tag{13}$$

$$K_e \frac{\partial T}{\partial r}|_{r=r_0} = -h_T(T_s - T_0) \text{ at t>0} \tag{14}$$

The fractional conversion for the whole pellet at any time is given by

$$X = 1 - \frac{3}{r_{g_0}^3 r_0^3}\int_0^{r_0} r_g^3 r^2 dr \tag{15}$$

Molar density of calcium carbonate (29.3kmol/m^3) is almost half the molar density of calcium oxide (59.2kmol/m^3) and hence there will be an increase in porosity during the reaction. The equation governing porosity change inside the pellet is given by

$$(1-\epsilon) = (1-\epsilon_0)\{z + \frac{r_g^3}{r_{g_0}^3}(1-z)\} \tag{16}$$

The effective diffusivity is given by (Murthy, 1994)

$$D_e = \frac{D_A}{\epsilon_0^{1/3}\tau_0}\{1 - (1-\epsilon_0)[z + \frac{r_g^3}{r_{g_0}^3}(1-z)]\}^{4/3} \tag{17}$$

and the effective thermal conductivity is given by

$$\begin{aligned}K_e =& K_B(1-\epsilon_0)[(1 - \frac{K_C}{K_B})\frac{r_g^3}{r_{g_0}^3} + \frac{K_C}{K_B}] \\ &[z + \frac{r_g^3}{r_{g_0}^3}(1-z)]\end{aligned} \tag{18}$$

The equations are nondimensionalised as per representation given in nomenclature.

Non Dimensional Equations

$$D_e = D_I F_D(\psi) \tag{19}$$

$$K_e = K_I F_K(\psi) \tag{20}$$

where

$$D_I = \frac{D_A}{\epsilon_0^{1/3}\tau_0} \tag{21}$$

$$F_D(\psi) = \{1-(1-\epsilon_0)[z+\psi^3(1-z)]\}^{4/3} \tag{22}$$

$$F_K(\psi) = (1-\epsilon_0)[(1-\lambda)\psi^3+\lambda][z+\psi^3(1-z)] \tag{23}$$

The governing partial differential equations become as

$$\begin{aligned}\frac{\partial\eta}{\partial\theta} =& \frac{\tau_4 F_D(\psi)}{\tau_3}[\frac{\partial^2\eta}{\partial\xi^2}+\frac{2}{\xi}\frac{\partial\eta}{\partial\xi}]+\frac{\tau_4}{\tau_1}\frac{Acos(\frac{\tau_4\theta}{\tau_1})}{(1+Asin(\frac{\tau_4\theta}{\tau_1}))}* \\ & [\frac{(\eta\phi-1)}{\phi}+\frac{\xi}{3}\frac{\partial\eta}{\partial\xi}]-\frac{\tau_4}{\tau_2}\frac{\psi^2}{\phi^3}e^{\alpha(1-\frac{1}{\omega})}\frac{(\eta-\eta_E)^n}{(1-\phi\eta_E)^n}\end{aligned} \tag{24}$$

$$\begin{aligned}\frac{\partial\omega}{\partial\theta} =& F_K(\psi)[\frac{\partial^2\omega}{\partial\xi^2}+\frac{2}{x}\xi\frac{\partial\omega}{\partial\xi}]+\frac{\tau_4\kappa v_0}{\tau_1}Acos(\frac{\tau_4\theta}{\tau_1})* \\ & [\omega+\frac{\xi}{3}\frac{\partial\omega}{\partial\xi}]-\frac{\tau_4}{\tau_2}\frac{\beta\psi^2}{\phi^3}e^{\alpha(1-\frac{1}{\omega})}\frac{(\eta-\eta_E)^n}{(1-\phi\eta_E)^n}\end{aligned} \tag{25}$$

$$\frac{\partial\psi}{\partial\theta} = -\frac{\tau_4}{\tau_2}\frac{\gamma}{\phi^2}e^{\alpha(1-\frac{1}{\omega})}\frac{(\eta-\eta_E)^n}{(1-\phi\eta_E)} \tag{26}$$

The initial and boundary conditions transform into

$$\eta = 0 \quad at \quad \theta = 0 \quad for \quad all \quad \xi \tag{27}$$

$$\omega = 1 \quad at \quad \theta = 0 \quad for \quad all \quad \xi \tag{28}$$

$$\psi = 1 \quad at \quad \theta = 0 \quad for \quad all \quad \xi \tag{29}$$

$$\frac{\partial\eta}{\partial\xi} = 0 \text{at } \xi = 0, \theta = 0 \tag{30}$$

$$\frac{\partial\omega}{\partial\xi} = 0 \text{at } \xi = 0, \theta = 0 \tag{31}$$

$$\frac{\partial\eta}{\partial\xi} = \frac{Bi_M}{F_D(\psi)}(1-\eta_s) at \xi = 1, \theta > 0 \tag{32}$$

$$\frac{\partial\omega}{\partial\xi} = \frac{Bi_H}{F_K(\psi)}(1-\omega_s)\xi = 1, \theta > 0 \tag{33}$$

The equation for fractional conversion can be written as

$$X = 1 - 3\int_0^1 \psi^3\xi^2 d\xi \tag{34}$$

3 Results

The equations in Section 2 above describe the variation of temperature, concentration, grain radius in terms of position and time. The nondimensionalised equations of Section 2 present the same picture in a more useful way since the parameters that appear can be estimated and so the relative importance of the processes at work can be identified from the time constants. In the present case

pulsing time τ_1 ($\frac{1}{2\pi f}$ = 1.4s), reaction time τ_2 ($\frac{1}{k}$ = 5x10^{-3}s), mass diffusion time for CO_2 τ_3 ($\frac{r_0^2}{D_e}$ = 5.66s) and thermal diffusion time τ_4 ($\frac{r_0^2 \rho C_p}{k_e}$ = 256s for $CaCO_3$ or 0.36 for CO_2) indicate that diffusional availability of heat in the solid is the slowest process. Accordingly the non dimensional time(θ) is defined on the basis of thermal diffusion time. Note that pulsing time can also be given as τ_5 = r_0/v where v (= $\frac{-r}{p}\frac{dp}{dt}$) is the velocity in pore space.

The nondimensional equations are converted into ordinary differential equations using central finite difference technique. Crank Nicholson technique, which is average of both explicit and implicit methods is used to solve the resulting ordinary differential equations (Golub and Ortega, 1992). Stability of numerical procedure is asserted by appropriate choice of step size in time and space.

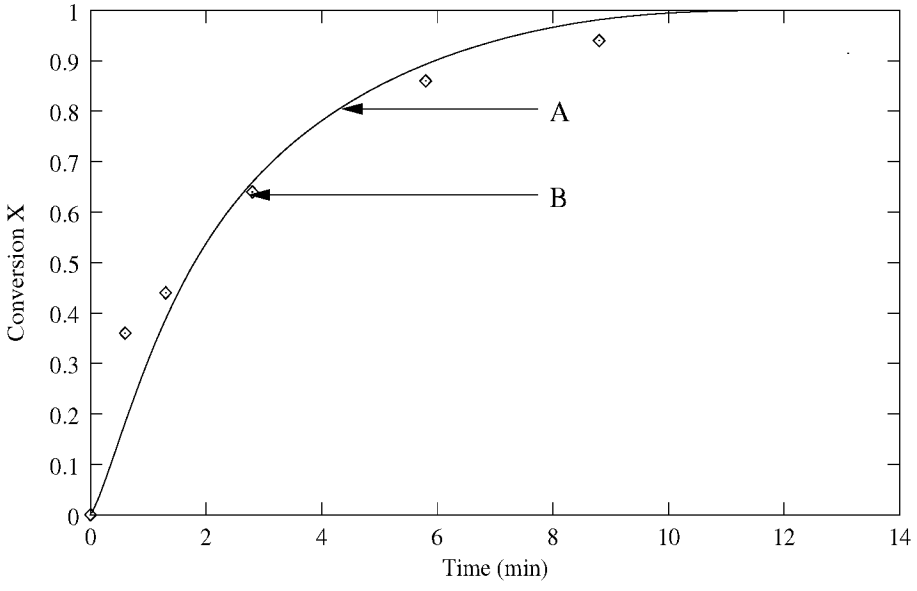

Figure 1: Conversion vs time profile for single pellet reduction of nickel oxide showing very good agreement between numerical result and experimental data, Curve A : Numerical, Curve B : Experimental (Sohn and Aboukheshem, 1992); Temperature of reaction = 653K, Amplitude of Pulsing (A) = 0.22, Frequency of pulsing (f) = 10Hz, Effective diffusivity (D_e) = 3.66x10$^{-5}m^2s^{-1}$, Reaction rate constant (k) = 1105x10$^{-6}m^3mol^{-1}s^{-1}$, Mole fraction of H_2 in bulk = 1.0

The numerical method used was verified by comparing the solution with analytical solution (Bailey and Ollis, 1986) for the case of unsteady heat transfer to solid spheres wherein excellent reproduction was obtained. The same numerical procedure was used to predict conversion time behaviour of nickel oxide reduction data of Sohn and Aboukheshem (1992) under pulsating flow. The prediction of instantaneous radial profile temperature and concentration are presented as time average over the pulsating time period τ_1. Figure 1 showing the good agreement between data and numerical predictions reveals that the numerical methods are satisfactory.

Figure 2 shows comparison between experimental data of Rao et al(1989) at 1150 K and predicted values of conversion-time relationship for calcium carbonate taking both material and

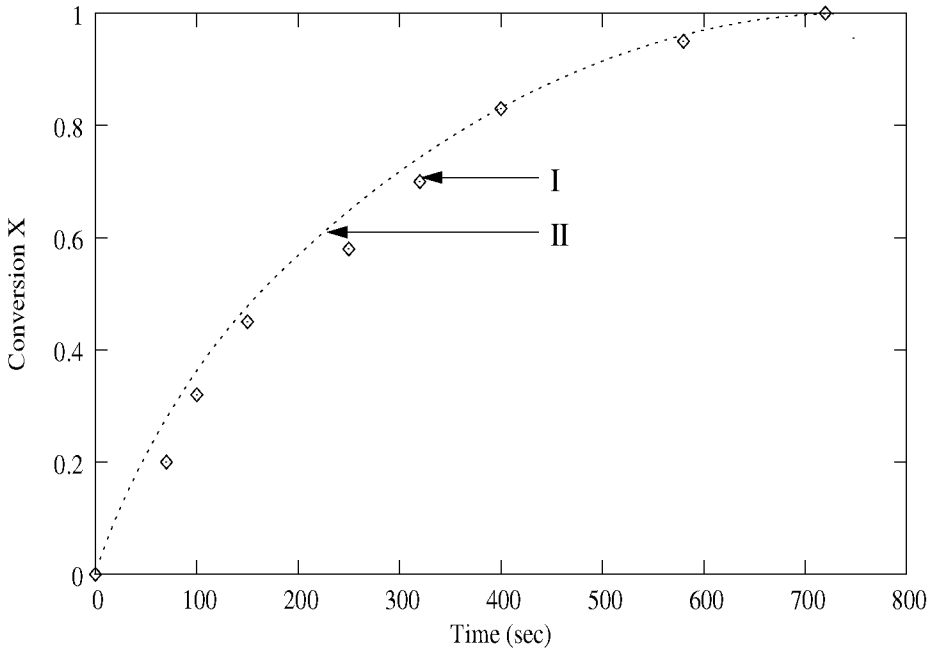

Figure 2: Conversion vs time profile for single pellet decomposition of $CaCO_3$ showing very good agreement between numerical result and experimental data, Curve I : Experimental (Rao et al., 1989), Curve II : Numerical; Pellet radius $r_p = 3.7\text{x}10^{-3}$m, Bulk temperature $T_0 = 1150$K, Grain radius $r_{g_0} = 5\text{x}10^{-6}$m, Diffusivity of CO_2 in $CaCO_3$ $D_a = 5.5\text{x}10^{-5}\text{m}^2/\text{s}$, Bulk concentration of CO_2 $C_{A_0} = 1.0\text{x}10^{-5}\text{kmol/m}^3$, Biot number for mass $B_{iM} = 3.5$, Biot number for heat $B_{iH} = 1.5$

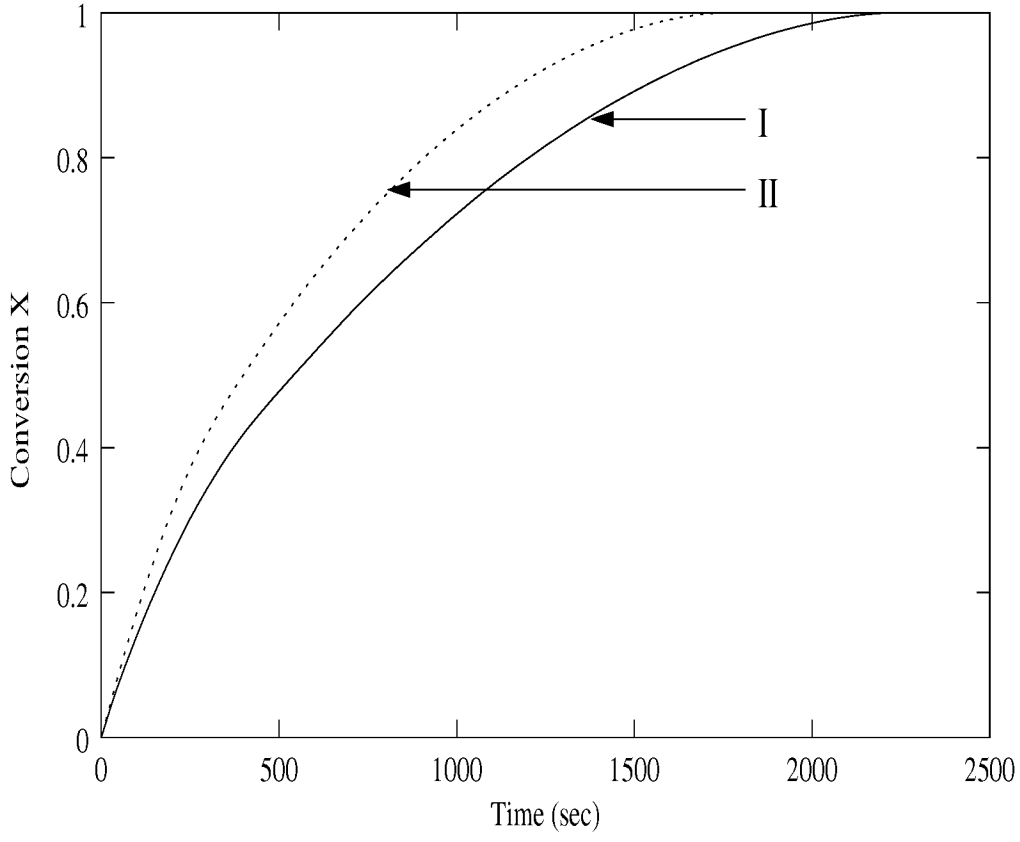

Figure 3: Single pellet prediction of conversion with time for grain model of solid $CaCO_3$ decomposition, Curve I (using Material and Energy balance equations) : Amplitude A = 0, Curve II (using only Material balance equations) : Amplitude A = 0.25, Frequency of pulsation f = 0.16Hz; Pellet radius $r_p = 6.0 \times 10^{-3}$m, Bulk temperature $T_0 = 1113$K, Grain radius $r_{g_0} = 3 \times 10^{-6}$m, Diffusivity of CO_2 in $CaCO_3$ $D_a = 4 \times 10^{-5}$m^2/s, Bulk concentration of CO_2 $C_{A_0} = 1 \times 10^{-5}$kmol/m^3, Biot number for mass $B_{iM} = 0.75$, Biot number for heat $B_{iH} = 2.0$

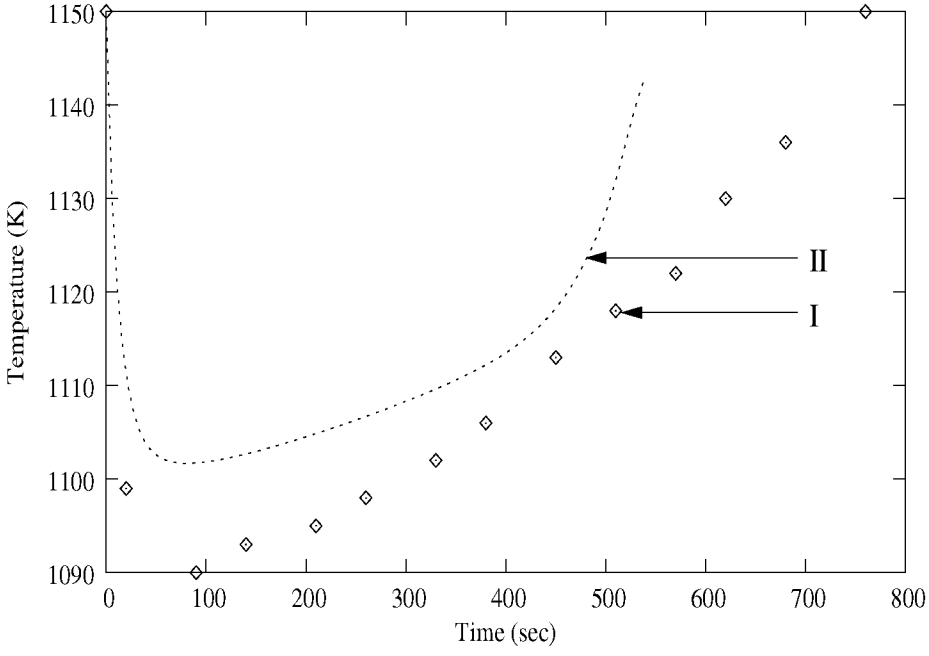

Figure 4: Temperature vs time profile for single pellet decomposition of $CaCO_3$ showing agreement between numerical result and experimental data, Curve I : Experimental (Rao et al., 1989), Curve II : Numerical; Pellet radius $r_p = 3.7\text{x}10^{-3}$m, Bulk temperature $T_0 = 1150$K, Grain radius $r_{g_0} = 5\text{x}10^{-6}$m, Diffusivity of CO_2 in $CaCO_3$ $D_a = 2.5\text{x}10^{-5}\text{m}^2/\text{s}$, Bulk concentration of CO_2 $C_{A_0} = 1.0\text{x}10^{-5}\text{kmol/m}^3$, Biot number for mass $B_{iM} = 3.5$, Biot number for heat $B_{iH} = 1.5$. The discrepancy between model prediction and data is due to inadequate information on system parameters.

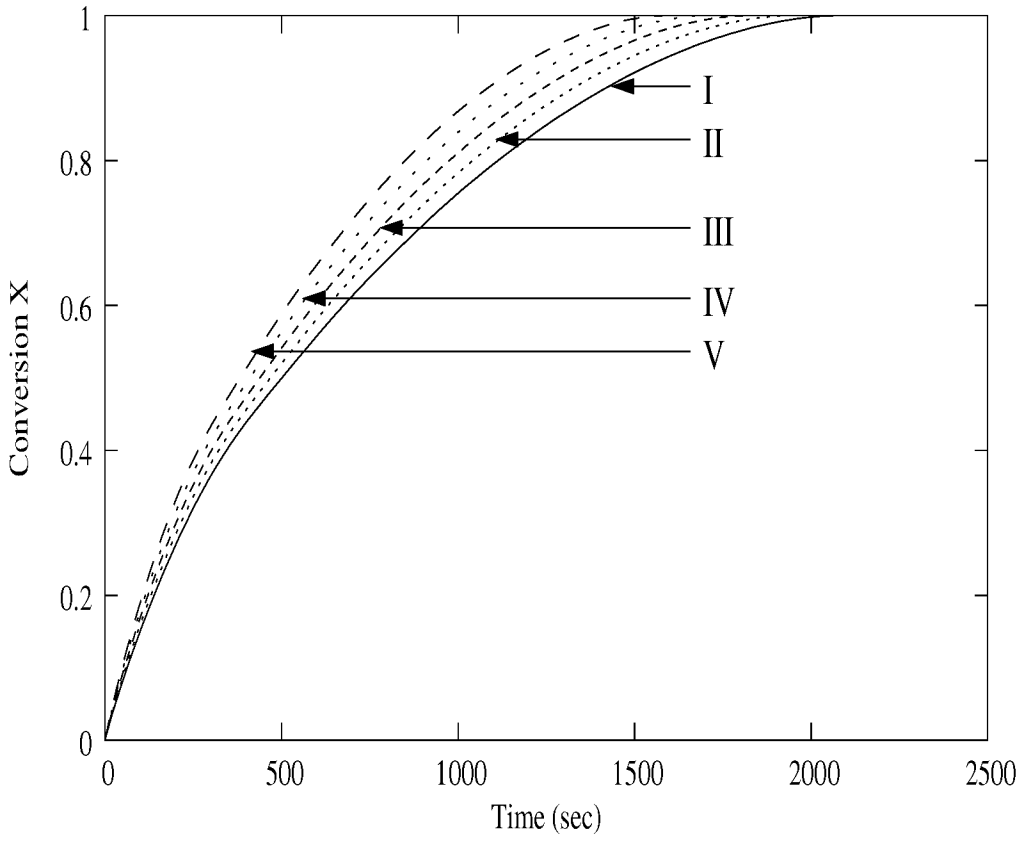

Figure 5: Effect of frequency for Single pellet prediction of conversion vs time for grain model of solid $CaCO_3$ decomposition showing higher conversion as frequency of pulsation is increased, Curve I : Frequency f = 0.08Hz, Curve II : Frequency f = 0.16Hz, Curve III : Frequency f = 0.32Hz, Curve IV : Frequency f = 0.64Hz, Curve V : Frequency f = 1.28Hz; Amplitude of pulsation A = 0.25, Pellet radius $r_p = 6.0\text{x}10^{-3}$m, Bulk temperature $T_0 = 1113$K, Grain radius $r_{g_0} = 6\text{x}10^{-6}$m, Diffusivity of CO_2 in $CaCO_3$ $D_a = 4\text{x}10^{-5}\text{m}^2/\text{s}$, Bulk concentration of CO_2 $C_{A_0} = 1\text{x}10^{-5}\text{kmol}/\text{m}^3$, Biot number for mass $B_{iM} = 2.0$, Biot number for heat $B_{iH} = 0.75$.

energy balance equations into account. Prediction of the same data using mass balance alone (not shown) was poor. Figure 3 illustrates differences in the predictions based on mass and energy balance (curve I) and mass balance alone (curve II); the lower conversion attained in curve I indicates that retention times depend upon heat energy availability for the endothermic reaction. Figure 4 shows comparison between experimental and predicted surface temperature-time profile; Results shows that temperature variation is small and is well packed up by model. The minor disagreement seen is due to inadequate knowledge of the parameter values of the data. Figure 5 shows the conversion-time predictions for different frequency. The time for complete conversion 2254 s for A=0 (=8.79 τ_4) to 1500 s at A = 0.25 and f=1.28 Hz is indicated . In view of the more favourable concentration of reactant in contact with pellet the observed decrease in the time required for reaction. Figures 6 and 7 show radial profiles of concentrations and temperature. These results reveal that A and f determnine bulk flow velocity (v = $\frac{-r}{p}\frac{dp}{dt}$) in pore space, hence the observed decrease in time required for reaction. Figure 8 shows radial temperature and Figure 9 shows concentration profiles for two situations viz I:solution of the system equation, II:solution of the system equations by deleting the pulsating term and adjusting the thermal conductivity (thermal diffusion coefficient) to fit the predictions of curve I. The approximate description obtained in II shows that for the situations up to f $\leq$ 0.16 and A $\leq$ 0.5 or equivalently a bulk flow velocity of 3.0 x 10^{-3}m/s, the approximation is satisfactory and the effect of pulsating term can be approximated by an equivalent apparent diffusion coeffcient. The results of Figures 6-9 show that the radial temperature variation is small $\simeq \Delta\omega$ 0.001-0.002 (ΔT$\simeq$1°C) indicating that the pellet is essentially at T_s.

Maity (1997) conducted experiments to study the effect of pulsating flow on limestone decomposition. He prepared pellets of $CaCO_3$ and coal mixture and combusted them in a packed bed with pulsating pressure across the bed. The heat for decomposition was provided by the burning coal. Temperature-time data was recorded at four different positions in the bed and extent of decomposition found at those positions by sampling. The values of the extent of dissociation for nonpulsating conditions ranged between 80-87% for those locations where the temperatures are higher than about 1000°C. The average ranged between 81-83%. On the other hand the average conversion values were almost always higher than 90% when the pressure was pulsated. Thus pressure pulsation increased the overall extent of reaction.

The experimental parameters of Maithy (1997) were applied to the present model and predictions of conversion vs time profiles were obtained. Table 2 gives the experimental and model results for decomposition under nonpulsating and pulsating conditions. Average time, temperature and conversion at the 4 positions where temperature and conversion was measured is taken and shown in Table 2. The temperature of reaction is taken equal to the average temperature measured for each run. Predicted conversion time profiles for single pellet case were found for different runs. Time required to achieve the experimental average conversion is also predicted and shown in Table 3. The results show consistency of model with experimental data. However experimental time (for X = X_{av}) higher than predicted time (for X = X_{av}) is indicated in Table 2; this implies that pellets are not at the average temperature indicated.

Table 3 summarizes the time constants for the processes taking place for three reactions : a) reduction of metal oxide data of Sohn and Aboukheshem (1992), b) Calcium carbonate decomposition, c)soya bean drying of Dias et al (2004). Experimental data of Sohn and Aboukheshem (1992) for metal oxide shows significant conversion-time improvement due to pulsating external pressure; while data of Dias et al (2004) for soya bean drying at 70 Hz shows no effect due to pulsating pressure. The above feature of the data can be explained from the time constants shown in Table 3.

In the case of Nickel oxide with highly non linear kinetics the process is controlled by diffusional resistance (τ_3, τ_4) and the small ratio τ_1/τ_3 of 0.001 brings about significant decrease in the overall resistance. In the case of soyabean drying, the process is controlled by bound moisture with τ_2 (= large) and so there is no effect; this feature perhaps arises from vapour pressure of condensed water in the capillaries being very low as per Kelvin equation. In the case of calcium carbonate decomposition which is controlled by thermal diffusion τ_4 (= 256 s) the ratio τ_1/τ_4 is 0.002, hence the observed similar results as that of NiO.

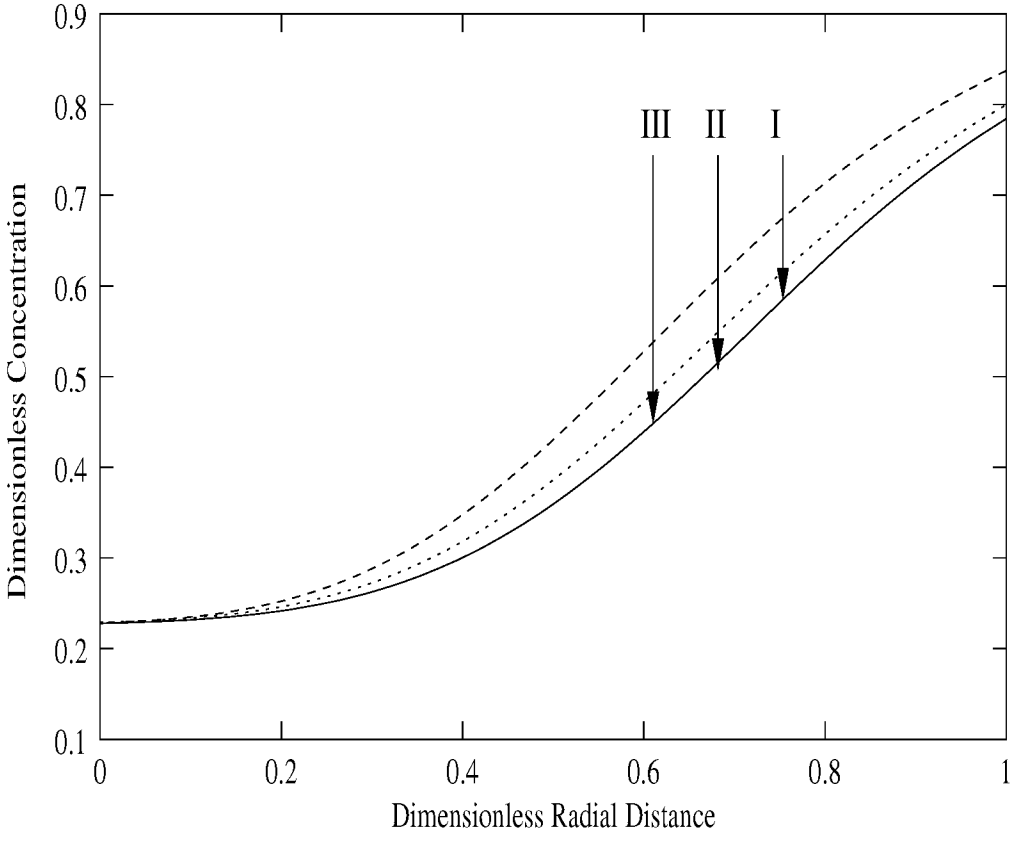

Figure 6: Single pellet prediction of dimensionless CO_2 concentration vs dimensionless radial for grain model of solid $CaCO_3$ decomposition for different amplitudes of pulsation 1556 sec after the start of reaction showing effect of pulsing amplitude on CO_2 concentration, Curve I : Amplitude A = 0, Curve II : Amplitude A = 0.25, Curve III : Amplitude A = 0.5; frequency of pulsation f = 0.16Hz, Pellet radius $r_p = 6.0 \times 10^{-3}$m, Bulk temperature $T_0 = 1113$K, Grain radius $r_{g_0} = 3 \times 10^{-6}$m, Diffusivity of CO_2 in $CaCO_3$ $D_a = 4 \times 10^{-5}$m^2/s, Bulk concentration of CO_2 $C_{A_0} = 1 \times 10^{-5}$kmol/m^3, Biot number for mass $B_{iM} = 0.75$, Biot number for heat $B_{iH} = 2$. Higher amplitude of pulsation enhances the diffusion of CO_2.

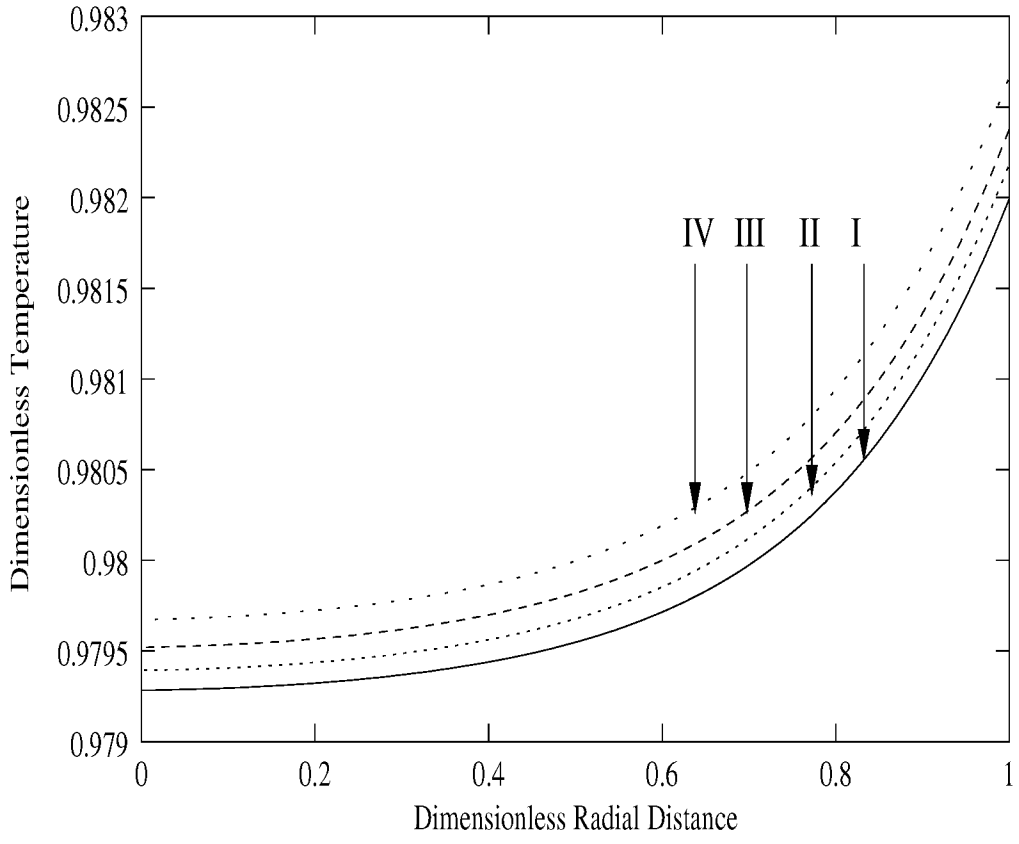

Figure 7: Single pellet prediction of dimensionless temperature vs dimensionless radial position of pellet for grain model of solid $CaCO_3$ decomposition for different frequencies of pulsation 286s after the start of reaction showing effect of pulsing frequency on temperature of pellet, Curve I : frequency f = 0.16Hz, Curve II : frequency f = 0.32Hz, Curve III : frequency f = 0.64Hz, Curve IV : frequency f = 1.28Hz, Amplitude of pulsation A = 0.25, Pellet radius $r_p = 6.0 \times 10^{-3}$m, Bulk temperature $T_0 = 1113$K, Grain radius $r_{g_0} = 3 \times 10^{-6}$m, Diffusivity of CO_2 in $CaCO_3$ $D_a = 4 \times 10^{-5}$m^2/s, Bulk concentration of CO_2 $C_{A_0} = 1 \times 10^{-5}$kmol/m^3, Biot number for mass $B_{iM} = 0.75$, Biot number for heat $B_{iH} = 2$. Higher frequency of pulsation enhances the diffusion of heat.

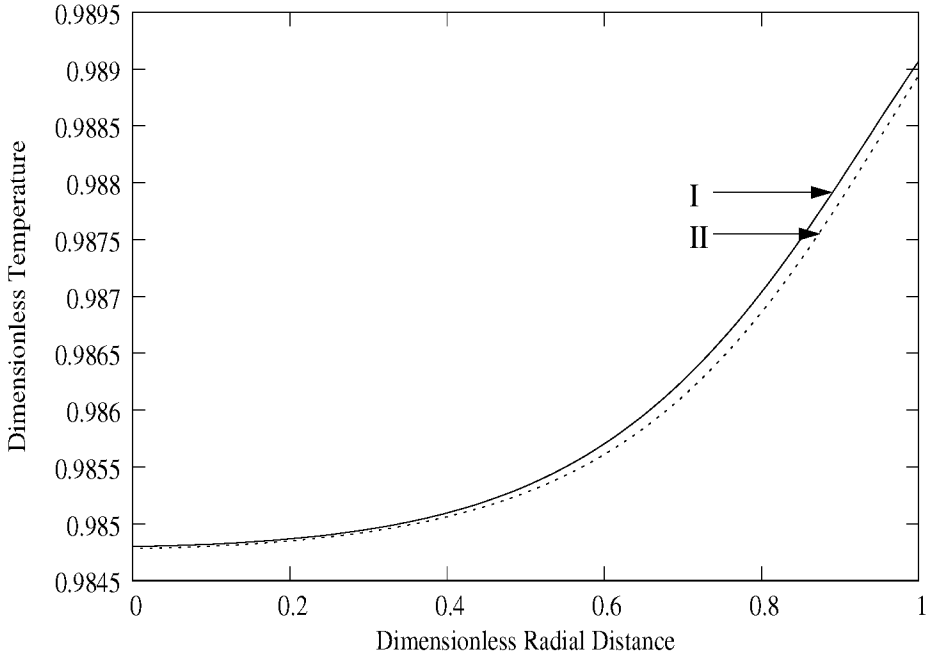

Figure 8: Radial temperature variation showing numerical solution curve I and approximate numerical solution curve II for single pellet decomposition of calcium carbonate modelling of pulsating pressure showing dimensionless temperature versus dimensionless radial distance, Curve I (pulsating pressure) : Amplitude A = 0.5, Frequency of Pulsation = 0.16Hz Thermal Conductivity K_B = 1.4J/mKs, Curve II (approximate solution by deleting pulsating pressure term by setting A=0 and adjusting thermal conductivity) : Amplitude A = 0.0, Thermal Conductivity K_B=1.5J/mKs; Pellet radius $r_p = 6.0 \times 10^{-3}$m, Bulk temperature T_0 = 1113K, Grain radius $r_{g_0} = 6 \times 10^{-6}$m, Diffusivity of CO_2 in $CaCO_3$ $D_a = 4 \times 10^{-5} m^2/s$, Bulk concentration of CO_2 $C_{A_0} = 1 \times 10^{-5}$kmol/$m^3$, Biot number for mass B_{iM} = 2.0, Biot number for heat B_{iH} = 0.75

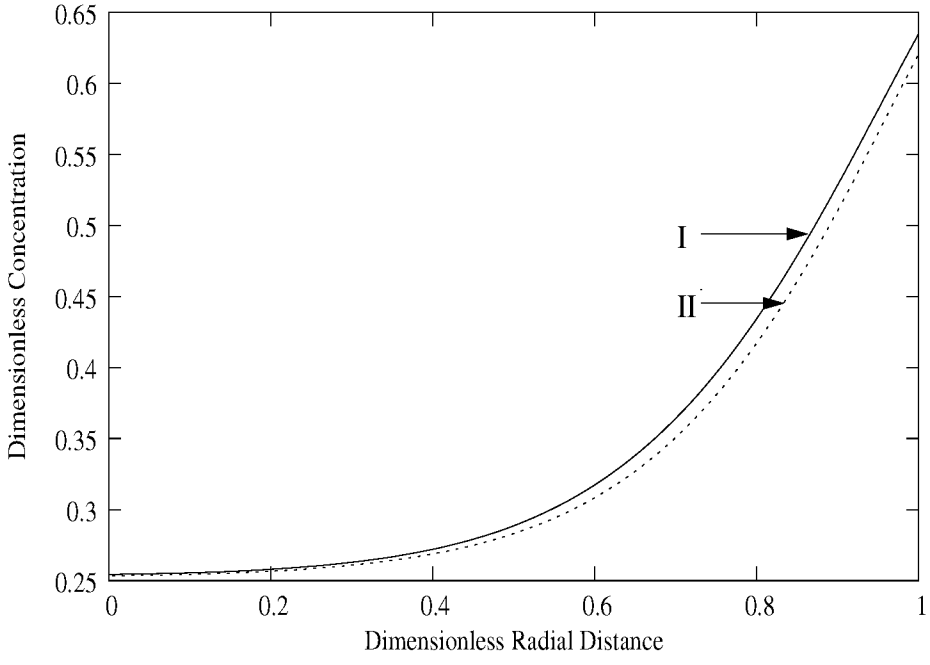

Figure 9: Radial concentration profile showing numerical solution curve I and approximate solution curve II for single pellet decomposition of calcium carbonate modelling of pulsating pressure showing dimensionless concentration versus dimensionless radial distance, Curve I : (pulsating pressure) Amplitude A = 0.5, Frequency of Pulsation = 0.16Hz Thermal Conductivity K $_B$ = 1.4J/mKs, Curve II : (approximate solution by deleting pulsating pressure term by setting A=0 and adjusting thermal conductivity) Amplitude A = 0.0, Thermal Conductivity K_B=1.5J/mKs; Pellet radius r_p = 6.0x10^{-3}m, Bulk temperature T_0 = 1113K, Grain radius r_{g_0} = 6x10^{-6}m, Diffusivity of CO_2 in $CaCO_3$ D_a = 4x10^{-5}m^2/s, Bulk concentration of CO_2 C_{A_0} = 1x10^{-5}kmol/m^3, Biot number for mass B_{iM} = 2.0, Biot number for heat B_{iH} = 0.75

Table 1: Values of different parameters used for decomposition of $CaCO_3$

ρ_B	29.3	kmol/m^3
ρ_C	59.2	kmol/m^3
n	2	-
C_p	1.268x10^5	J/kmolK
D_A	2x10^{-5}	^{2}/s
ΔH	1.78x10^8	J/kmol
E	1.75x10^5	J/mol
K_B	1.4	J/mKs
K_C	7	J/mKs
K_{r0}	2.45x10^{-5}	kmol/m^{2}s
R_g	8.314	J/molK
C_{A0}	1x10^-5	kmol/m^3
ϵ_0	0.63	-
r_{g_0}	3x10^{-6}	m
r_0	5.975x10^{-3}	m
T_0	1113	K
τ_0	2	-
f	$1/2\pi$	Hz
h_T	58.5	J/m^{2}Ks
k_g	5x10^{-3}	m/s
$\Delta\xi$	-0.1	-
$\Delta\theta$	0.000001	-
C_{E0}	4.5x10^{-3}	kmol/m^3
B_{iM}	1.5	-
B_{iH}	0.25	-
κ	0.253	-
α	18.99	-
v_0	3.69x10^{-4}	-
β	1.97x10^{-4}	-
τ_1	1	s
τ_2	5.04x10^{-3}	s
τ_3	5.66	s
τ_4	256.05	s

Table 2: Comparison of packed bed experimental data of Maity (1997) and predictions of single pellet model of Patil (2004)

No	A	f	T_{avg}	X_{avg}	$Time_{avg}$	$Time_{predicted}$	$Time_{predicted}$
		Hz	°C	% (experimental)	s (experimental)	s (for X=100%)	s (for X=X_{avg}
1	0	-	900	79	129	560	95
2	0	-	1057	81	115	203	107
3	0	-	1121	81	133	199	100
4	0	-	1178	83	140	140	73
5	0	-	1186	83	137	131	65
6	0	-	1321	81	116	110	53
7	0.125	0.3	1146	92.5	160	141	93
8	0.125	0.33	1089	90	160	169	106
9	0.125	0.33	1140	92.5	223	141	94
10	0.125	0.33	1146	92.5	160	141	93
11	0.125	0.33	1252	83	112	114	56
12	0.125	0.75	1256	95	115	253	191
13	0.125	1.25	1292	94.5	111	190	138
14	0.125	0.33	1302	94	164	106	68
15	0.125	0.75	1345	96.3	119	162	123

Table 3: Time constants for some systems where τ_1 or τ_5 :pulsing time, τ_2:reaction time, τ_3:mass diffusion time, τ_4:thermal diffusion time. Diffusion times τ_3 refer to H_2/ H_2O mixture in NiO; CO_2 in $CaCO_3$ decomposition and water vapour for soya drying.

system	r_0	T	τ_1	τ_2	τ_3	τ_4	τ_5	source
	m	K	s	s	s	s	s	
NiO	0.01	573	0.03	0.385	33	10	0.04	Gandi (2004)
$CaCO_3$	0.006	1150	0.55	0.005	5.66	256	4	Patil (2004)
soyabean	0.01	333	0.002	$4x10^7$	10	160	0.008	Gandi (2004)

4 Conclusion

The work presented leads to following conclusions:

1. Calcium carbonate decomposition, temperature gradient in the pellet is small and that heat supply is the rate controlling step.
2. The effect of pulsating convective flow on temperature and concentration profile can be described approximately for small velocities v < 3mm/s by diffusion-reaction model with a higher value diffusion coefficient and without the pulsating convection term.
3. Pulsating pressure is useful if the diffusion time is a significant component of the overall reaction time.

Nomenclature

A	Dimensionless amplitude of pressure cycling
B_{iH}	Biot number for heat $\frac{h_T r_0}{K_I}$
B_{iM}	Biot number for mass $\frac{k_g r_0}{D_I}$
C_A	Concentration of reactant gas A $(kmol/m^3)$
C_{A0}	Concentration of reactant gas A initially $(kmol/m^3)$
C_{As}	Concentration of reactant gas A at surface $(kmol/m^3)$
C_E	Concentration of CO_2 in equilibrium with solid at any time and radial position$(kmol/m^3)$
C_{E0}	Concentration of CO_2 in equilibrium with solid at any radial position initially$(kmol/m^3)$
C_p	Molar specific heat of ($CaCO_3$) $(kmol/m^3)$
C_{pa}	Molar specific heat of air $(kmol/m^3)$
D_A	Bulk diffusivity (m^2/s)
D_e	Effective diffusivity (m^2/s)
D_I	Initial diffusivity (m^2/s)
f	Frequency of pulsing (Hz)
h_T	Total heat transfer coefficient (J/m^2Ks)
k_g	Mass transfer coefficient (m/s)
K_B	Thermal conductivity of $CaCO_3$ (J/mKs)
K_C	Thermal conductivity of CaO (J/mKs)
K_e	Effective thermal conductivity (J/mKs)
K_I	Initial thermal conductivity of $CaCO_3$ (J/mKs)
K_r	Reaction rate constant $(kmol/m^2s)$
n	Order of reaction
p	Total pressure (N/m^2)
p_E	Equilibrium partial pressure of $CO_2(N/m^2)$
r	Radial position at any given time (m)
r_0	Initial radius of pellet (m)
r_g	Average radius of grains (m)
r_{g0}	Initial average radius of grains (m)
t	Time (s)
T	Absolute temperature (K)
T_0	Bulk gas temperature (K)
T_s	Temperature at pellet surface (K)
v	velocity (m/s)
v_0	$\frac{p_0}{\rho_p R T_0}$
X	Conversion
z	Ratio of molar density of $CaCO_3$ to molar density of CaO
α	$\frac{E}{RT}$
ϕ	1-$\frac{C_{A0}}{C_{E0}}$
ΔH	Heat of reaction $(J/kmol)$
Δr	Step size in radial position (m)
ϵ_0	Initial porosity of pellet
ϵ	Porosity of pellet
η	Dimensionless concentration of CO_2 $\frac{1}{\phi}$(1-$\frac{C_A}{C_{E0}}$)
η_E	Dimensionless equilibrium gas concentration of CO_2 $\frac{1}{\phi}$(1-$\frac{C_E}{C_{E0}}$)
η_s	Dimensionless equilibrium concentration of CO_2 at surface of pellet
θ	Dimensionless time $\frac{t}{\tau_4}$
ξ	Dimensionless radial distance $\frac{r}{r_0}$
ρ	Molar density $(kmol/m^3)$
ρ_B	Molar density of $CaCO_3$ $(kmol/m^3)$
ρ_C	Molar density of CaO $(kmol/m^3)$

ρ_p Molar density of pellet $(kmol/m^3)$
τ_0 Initial tortuosity factor
τ_1 Pulsing time $\frac{1}{2\pi f}$ (s)
τ_2 Reaction time $\frac{C_{E0} r_{g0}}{3(1-\epsilon_0)K_{r0}}$ (s)
τ_3 Mass Diffusion time $\frac{r_0^2}{D_I}$ (s)
τ_4 Thermal diffusion time $\frac{\rho_p C_p r_0^2}{K_I}$ (s)
τ_5 Pulsing time (r_0/v) (s)
ψ Dimensionless radius of grain $\frac{r_g}{r_{g0}}$
ω Dimensionless temperature $\frac{T}{T_0}$
ω_s Dimensionless temperature at surface of pellet
γ $\frac{C_{E0}}{3(1-\epsilon_0)\rho_B}$
κ $\frac{C_{pa}}{C_p}$
λ $\frac{K_C}{K_B}$
β $\frac{\Delta H C_{E0}}{\rho_p C_p T_0}$

References

Ballal, N. B., 1995, Mass Transfer in Porous Solids Under Pulsating Pressure Conditions, *ISIJ International*, **258**, pp 446-448.

Bailey, J. E. and Ollis, D. F., 1986, Biochemical Engineering Fundamentals, McGrawHill, NewYork.

Dias, S.R.S., Futata, F.P.L., Carvalho, J.A., Couto, H.S. and Feireira, M.A., 2004, Investigation of food drying with pulsating flow, *International Commn Heat and Mass Transfer* , **31**, pp 387-395.

Frankel, S. L. and Nogueria, L. A. H., 1998, Heat Transfer Coefficients for Drying in Pulsating FLow, *International Commn Heat and Mass Transfer*, **25**, pp 471-480.

Gandi, R.K., Studies in Calcium carbonate decomposition under pulsating external pressure, M.Tech Thesis, Department of Chemical Engineering, IIT Bombay, July 2004.

Golub, G. H. and Ortega, J. M., 1992, Scientific Computing and Differential Equations.

Hamer, W. J. and Cormack, E. D., 1978, Influence of Oscillating External Pressure on Gas Phase Reactions in Porous Catalysts, *Chemical Engineering Science*, **33**, pp 935-944.

Hill, K. J. and Winter, E. R. S., 1956, Thermal Dissociation Pressure of Calcium Carbonate, *J. phys. Chem.*, **60**, pp 1361-1362.

Ingraham, T. R. and Marrier, P., 1963, Chemical Kinetics on the Thermal Decomposition of Calcium Carbonate, *Canadian Journal of Chemical Engineering*, **41**, pp 170-173.

Maithy, S. K., 1997, Effect of pressure pulsation on gas solid reaction in packed beds, *M.Tech. Thesis, Department of Metallurgical Engineering and Material Sciences, Indian Institute of Technology, Bombay*

Murthy, M. S., Harish, B. R., Rajanandam, K. S. and Ajoy Pavan Kumar, K. Y., 1994, Investigation on the Kinetics of Thermal Decomposition of Calcium Carbonate, *Chemical Engineering Science*, **49**, pp 2198-2204.

Narsimhan, G., 1961, Thermal Decomposition of Calcium Carbonate, *Chemical Engineering Science*, **16**, pp 7-20.

Ohmi, M. and Usui, T., 1976b, Therotical Investigation of Reaction Kinetics in the Reduction of Single Hematite Pellet Under Flow of Hydrogen, *Transcations ISIJ*, **16**, pp 85-91.

Patil, K., Studies in Calcium carbonate decomposition under pulsating external pressure, Dual Degree M.Tech thesis, Department of Chemical Engineering, IIT Bombay, July 2004.

Rajeswara Rao, T., Gunn, D. J. and Bowen, J. H., 1989, Kinetics of Calcium Carbonate Decomposition, *Chem Engg Res Des*, **67**, pp 38-47.

Satterfield, C. N. and Feakes, F., 1959, Kinetics of Thermal Decomposition of Calcium Carbonate, *A.I.Ch.E. J.*, **5**, pp 115-122.

Sohn, H. Y. and Aboukheshem, M. B., 1992, Gas-Solid Reaction-Rate Enhancement by Pressure Cycling, *Metalurgical Transactions B*, **23B**, pp 285-294.

Sohn, H. Y. and Chaubal, P. C., 1984, Rate Enhancement of the Gaseous Reduction of Iron Oxide Pellets by Pressure Cycling, *ISIJ* , **24**, pp 387-395.